minerals

MDPI

Article

Remote Sensing, Petrological and Geochemical Data for Lithological Mapping in Wadi Kid, Southeast Sinai, Egypt

Wael Fahmy [1], Hatem M. El-Desoky [1], Mahmoud H. Elyaseer [1], Patrick Ayonta Kenne [2], Aref Shirazi [3,*], Ardeshir Hezarkhani [3], Adel Shirazy [3], Hamada El-Awny [1], Ahmed M. Abdel-Rahman [1], Ahmed E. Khalil [4], Ahmed Eraky [1] and Amin Beiranvand Pour [5,*]

[1] Geology Department, Faculty of Science, Al-Azhar University, Nasr City 11884, Egypt; kady2040@azhar.edu.eg (A.M.A.-R.); ahmederaky417@gmail.com (A.E.)
[2] Department of Earth Sciences, University of Dschang, Dschang P.O. Box 96, Cameroon
[3] Department of Mining Engineering, Amirkabir University of Technology, Tehran 1591634311, Iran; adel.shirazy@aut.ac.ir (A.S.)
[4] Department of Geology, National Research Center, Cairo 12622, Egypt
[5] Institute of Oceanography and Environment (INOS), University Malaysia Terengganu (UMT), Kuala Nerus 21030, Terengganu, Malaysia
* Correspondence: aref.shirazi@aut.ac.ir (A.S.); beiranvand.pour@umt.edu.my (A.B.P.); Tel.: +98-21-6454-2968 (A.S.); +60-9-668-3824 (A.B.P.); Fax: +98-21-6640-5846 (A.S.); +60-9-669-2166 (A.B.P.)

Abstract: The Wadi Samra–Wadi Kid district in southeastern Sinai, Egypt, has undergone extensive investigation involving remote sensing analysis, field geology studies, petrography, and geochemistry. The main aim of this study is the integration between remote sensing applications, fieldwork, and laboratory studies for accurate lithological mapping for future mineral exploration in the study region. The field relationships between these coincident rocks were studied in the study area. Landsat-8 (OLI) data that cover the investigated area were used in this paper. The different rock units in the study area were studied petrographically using a polarizing microscope, in addition to major and trace analysis using ICP-OES tools. The Operational Land Imager (OLI) images were used with several processing methods, such as false color composite (FCC), band ratio (BR), principal component analysis (PCA), and minimum noise fraction (MNF) techniques for detecting the different types of rock units in the Wadi Kid district. This district mainly consists of a volcano-sedimentary sequence as well as diorite, gabbro, granite, and albitite. Geochemically, the metasediments are classified as pelitic graywackes derived from sedimentary origin (i.e., shales). The Al_2O_3 and CaO contents are medium–high, while the Fe_2O_3 and TiO_2 contents are very low. Alkaline minerals are relatively low–medium in content. All of the metasediment samples are characterized by high MgO contents and low SiO_2, Fe_2O_3, and CaO contents. The granitic rocks appear to have alkaline and subalkaline affinity, while the subalkaline granites are high-K calc-alkaline to shoshonite series. The alkaline rocks are classified as albitite, while the calc-alkaline series samples vary from monzodiorites to granites. The outcomes of this study can be used for prospecting metallic and industrial mineral exploration in the Wadi Kid district.

Keywords: remote sensing; Operational Land Imager (OLI); petrology; geochemistry; Wadi Kid; metasediments; albitite

check for updates

Citation: Fahmy, W.; El-Desoky, H.M.; Elyaseer, M.H.; Ayonta Kenne, P.; Shirazi, A.; Hezarkhani, A.; Shirazy, A.; El-Awny, H.; Abdel-Rahman, A.M.; Khalil, A.E.; et al. Remote Sensing, Petrological and Geochemical Data for Lithological Mapping in Wadi Kid, Southeast Sinai, Egypt. *Minerals* **2023**, *13*, 1160. https://doi.org/10.3390/min13091160

Academic Editor: Denis Thiéblemont

Received: 10 July 2023
Revised: 4 August 2023
Accepted: 29 August 2023
Published: 31 August 2023

1. Introduction

Geological mapping plays a vital role in understanding the Earth's surface and subsurface characteristics. On a global scale, many forms of mapping and the detection of alterations in mineralized zones have been effectively accomplished using remote sensing and GIS approaches. Remote sensing techniques offer valuable tools for such mapping, allowing for efficient data acquisition and analysis over vast regions. For lithological, structural, and mineralogical mapping, ASTER, Landsat-8, and Sentinel-2 data have been extensively employed [1–5]. Remotely sensed spectral photography shows great promise for overcoming the logistical and financial constraints associated with conventional field-based geological mapping over large areas [6,7]. The most effective uses of satellite imagery for mineral exploration are hydrothermal mineral detection and mapping, lithological discrimination, and lineament analysis [8–10]. Several researchers have utilized Landsat-8 and ASTER data to distinguish lithological mapping and hydrothermal alteration zones for exploring mineral discoveries (e.g., [11–25]).

The Arabian–Nubian Shield (ANS) is one of the largest blocs of Neoproterozoic juvenile continental crust [26]. This shield was formed between 900 Ma and 550 Ma and is characterized by many crustal growths, including intra-oceanic magmatism, the amalgamation of arc complexes, and collisions between the eastern and western blocks of Gondwana [27–36]. The basement complex of Egypt, especially the Sinai Peninsula, is a part of the Arabian–Nubian Shield (ANS). This area can be divided into three groups, from oldest to youngest: (1) a metamorphic unit made up of low- to medium-metamorphosed volcano-sedimentary rocks, (2) calc-alkaline granites, and (3) within-plate granites (e.g., [37–43]). However, the distribution of granitoids within this area is not homogeneous. Several works indicate an "older Granite suite" (OGS) ranging between quartz diorite and granodiorite, formed during active subduction processes [44,45], and a younger granite suite (YGS) made up of calc-alkaline I-type granites and A-type granites that are strongly peraluminous to slightly metaluminous in composition. The younger rocks are mostly alkali feldspar granites, syenogranites, and monzogranites, associated with mafic plutons or dykes [45–47]. A few but no less important rocks, like A-type granites, have also been identified within the younger granites and are thought to have been emplaced in anorogenic extensional within-plate settings (e.g., [48–50]). However, recent studies have shown that the emplacement of these rocks was almost coeval with the ages (610–590) of the younger granites (e.g., [51–53]). The petrogenesis of A-type granites and their relationship with younger granites remain poorly constrained.

The Wadi Kid district, located in the southern part of the Sinai Peninsula, belongs to the Kid metamorphic complex [54]. These rocks underwent polyphase deformation and low-pressure metamorphism, ranging in grade from greenschist facies in the south to amphibolite facies in the center and the north [54–58]. This area is also characterized by many metasedimentary rocks and granitic plutons associated with A-type rocks, as well as basic rocks. In this contribution, detailed field mapping and petrographic studies associated with major and trace data for the spatial association of granitic rocks and A-type granites were conducted to constrain their sources, their tectonic environment, and their petrogenetic processes. The major goals of the current study were to understand the geochemical affinity, petrogenesis, and geological context of the exposed rock sections. The numerous rock units in the research region were lithologically differentiated using remote sensing and GIS methods.

2. Geological Background

From a geological perspective, the Sinai Peninsula is the most appealing area in Egypt. This peninsula is situated between the Mediterranean Sea to the north and the Red Sea to the south, the Suez Gulf to the west, and the Aqaba Gulf to the east. Its triangular shape, which was inspired by the Mediterranean shoreline, has an apex created by the union of two Gulfs: Aqaba and Suez. The southern part of Sinai is formed of a complicated system of rough peaks that are composed of igneous and metamorphic materials. Geographically, this region is distinguished by highlands in the north and mountains in the south, with St. Catherine at 2640 m above sea level being the highest mountain peak.

The Kid Metamorphic Complex (KMC) is composed of volcano-sedimentary sequences, as well as migmatites, diorites, and granite plutons that form a dome structure of about 600 km^2 located along Wadi Kid in southeast Sinai (Figure 1). Post-collisional granitoids can also be observed in the study area [52]. The mapping of the Wadi Kid Complex and stratigraphic division of the sequence were studied in previous works [59,60].

Sinai metasediments occur as sedimentary successions within the volcano-sedimentary sequences of the KMC. According to [61], the Wadi Kid region has relatively thin, lengthy, severely deformed bands of sedimentary and volcanic rocks that divide the Midyan terrane from a portion of the Gerf terrane. The metamorphic grade increases from the south toward the west–central and northern parts of the complex [58].

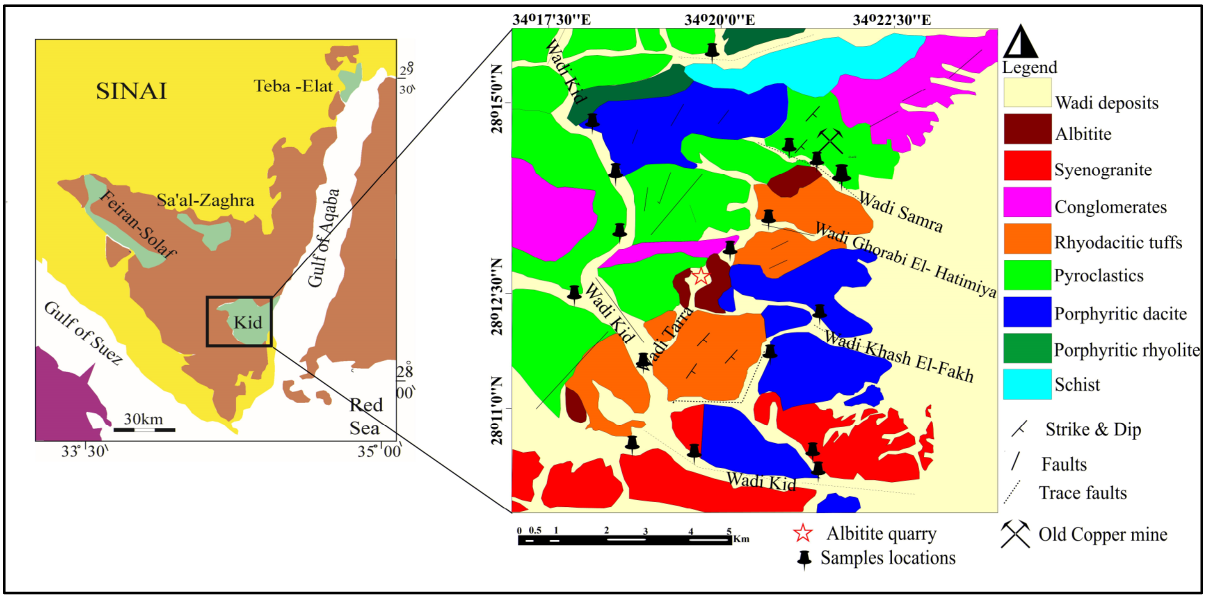

Figure 1. Geological map of the Wadi Kid district, southeast Sinai, Egypt (modified after [62,63]).

The northern part is made up of the Um Zariq and Malhaq formations. This area displays metamorphosed and amphibolite-grade facies. The Um Zariq formation is dominated by quartz-rich metapelites and metapsammites (e.g., graphitic phyllites and mica schists) that are interbedded with lithic metagraywackes, related metatuffs, and minor lavas of silicic and intermediate composition [54]. These rocks have been considered to be formed during an active continental margin [64]. The Malhaq formation comprises a series of metavolcanic rocks of mainly acidic-to-intermediate varieties with minor basic composition [65,66]. This formation includes vesicular lavas, pyroclastic and finely bedded tuffs, and their derived sediments of conglomerates, pebbly graywackes, and pelites. It has been described as back arc/arc-related calc-alkaline volcanic rocks and sediments [55].

The central Kid district is dominated by low-grade metamorphosed rocks, which are mixed sequences of metasediments and metavolcanic rocks. The metasediments' succession contains a significantly thick sequence of turbiditic slate and graywacke (Beda turbidites) with cobble and boulder conglomerate beds. The rocks display a lower metamorphic grade than the Um Zariq and Malhaq formations and are less deformed. Ref. [55] shows that the rocks were formed in an island-arc–volcanic environment and deposited in a marine environment.

The southeastern part of the Kid complex consists of the variable lithologies of the Tarr complex. These include low-grade metamorphosed dacitic–andesitic lavas, ignimbrites, volcanic breccias and tuffs, pebbly mudstones, and impure carbonates. These rocks depict greenschist facies conditions of 300 °C and P 2 k bars, but up to 550 °C [65,66]. Several studies [67–69] have shown that the metasediments and metavolcanic rocks display an age of 610–615 Ma for the Wadi Kid district. Also, a weighted mean 206Pb/238U age of 615 ± 6 Ma was obtained for Kid metasediments. The most important feature in this area is a small intrusion of albitites.

3. Materials and Methods

3.1. Remote Sensing Data

Landsat-8 (OLI) data that cover the investigated area were used in this paper. Landsat-8 is equipped with two instruments: the Operational Land Imager (OLI) and the Thermal Infrared Sensor (TIRS). The OLI is represented by 9 bands, while the TIRS data only provide 2 bands. On 28 September 2021, the scene that encompasses the investigation region was path 174 and row 40. The projection system of the Landsat-8 image is the UTM (Universal Transverse Mercator), Zone N36, related to the WGS-84 datum. The Landsat-8 image underwent a number of processing techniques for lithological mapping, including false color composite (FCC), principal component analysis (PCA), minimum noise fraction (MNF), and band ratio (BR) [70]. The integration of Landsat-8 (OLI) and ASTER data, along with laboratory analysis, is presented in the given flowchart (Figure 2).

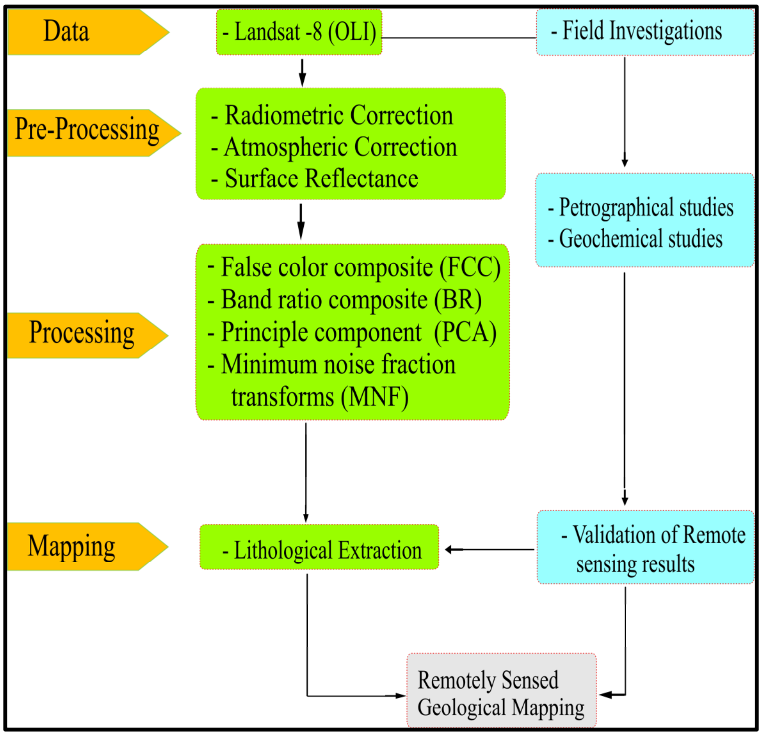

Figure 2. Flowchart illustrating the integration of the used methodology in the studied area.

3.1.1. Preprocessing

Remote sensing images downloaded from the USGS website (http://earthexplorer.usgs.gov) were preprocessed by the data providers. The Landsat-8 image was processed to level 1 terrain-corrected (L1T), which is radiometrically, geometrically, and topographically accurate [71]. To preprocess the OLI data and correct for atmospheric, solar, and topographic effects, several steps were followed. The first step was radiometric calibration, which involved calibrating the data to radiance or top-of-atmosphere reflectance. This step took into account the Earth–Sun relationship, time of day, and year. The second step involved using the Fast Line-of-Sight Atmospheric Analysis of Spectral Hypercubes (FLAASH) algorithm [72] for atmospheric correction. To process the multispectral images digitally, ENVI software version 5.1 was used. This software is a complete digital processing program capable of carrying out preprocessing, enhancement, transformation, and classification of remote sensing images. These processes were used to extract spatial and spectral information related to geology, such as lithological mapping. Finally, ArcGIS 10 was used for some processing and finalization.

3.1.2. Image Processing Techniques

In the realm of geological analysis and remote sensing, the use of multispectral data derived from OLI images offers a wealth of diverse spectral information. Surprisingly, a mere three bands are sufficient to create visually captivating color images by combining them to represent the red (R), green (G), and blue (B) channels, commonly known as RGB. The challenge lies in selecting the most optimal band combinations that reduce information redundancy, highlight desired features, and minimize correlations between bands [73]. To address these requirements, principal component analysis (PCA) emerges as a fundamental multivariate statistical method [74]. By transforming the data, PCA effectively separates noise components and reduces spectral dimensionality, producing uncorrelated output bands. Additionally, the minimum noise fraction (MNF) technique comes into play, further reducing dataset dimensionality while preserving important noise-free components, resulting in efficient subsequent processing with reduced computational demand [75]. Another powerful image processing tool, the band ratio technique, proves invaluable in accentuating anomalies and enhancing spectral differences between surface materials. Importantly, it effectively suppresses unwanted information, such as changes in scene illumination conditions [75]. This study leverages the band ratio technique to advance the discrimination between distinct rock units, paving the way for enhanced geological insights [76–79].

3.2. Field and Laboratory Investigations

The following points summarize the field and laboratory investigations carried out for this research work:

1. Fieldwork conducted during the field investigation (which lasted seven days) included sampling and description of field relations and structural settings of the rock units exposed in the study area, particularly metasediments, Shahira gabbros, diorites, granitic rocks, albitites, and aplitic dykes.
2. The assessment of the lithology of the different rock units in the study district was based on petrographical studies of about 35 thin sections using the polarizing microscope at the Laboratories of Al-Azhar University.
3. Eighteen representative rock samples were chemically analyzed for major and trace elements at the laboratories of the National Research Center, Dokki, Egypt. In the study area, the samples were procured from 5 samples of diorite, 6 samples of granite, 2 samples of albitite, and 5 samples of metasediments. Following a lithium metaborate/tetraborate fusion and diluted nitric digestion, a 0.2 g sample was analyzed by ICP-OES to determine the total abundances of the main oxides and a number of minor elements. Common oxides for each element were used to express them, such as Al_2O_3, CaO, Fe_2O_3, K_2O, MgO, MnO, Na_2O, P_2O_5, and TiO_2. One gram of each sample was heated for 90 min at 950 °C to determine the loss on ignition (L.O.I.), and the weight loss that occurred during this procedure was converted to L.O.I. ICP-OES was used to determine the trace elements (Cr, Co, Sr, Zr, Nb, Cu, Pb, Zn, Y, Ga, and Ce). The categorization, nomenclature, magma type, and tectonic setting of the studied rocks in the research region were ascertained using the geochemistry (Minpet) program and the current data.

4. Results and Discussion

4.1. Remote Sensing

4.1.1. False Color Composite (FCC)

In order to display the various rock units in the study area, the Optimum Index Factor (OIF) technique was employed to select the most suitable false color composite (FCC) from the available data. The histogram showcases the min/max/mean reflectance values of the OLI multispectral bands, offering a comprehensive overview of the spectral properties utilized in our study (Figure 3). The analysis of the OIF results showed a combination of OLI data for enhancing lithological rock units (Table 1). There were six combinations of bands as a result of the relationships between the standard deviations and correlation coefficients of the OIF calculations [80,81]. For better extraction of lithological information, triplets of higher band combination values were used, since they use bands with the highest variance and least redundancy in OLI images (b7, b6, b1) in RGB (Figure 4a). The FCC combinations (7, 5, and 1) in RGB (Figure 4b) were selected for the best visual interpretation and lithological differentiation of different rock units in the investigated area.

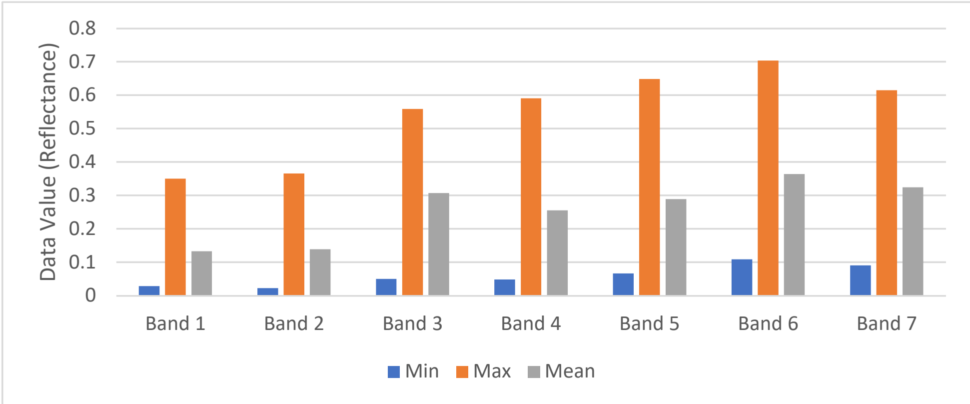

Figure 3. Histogram for the min/max/mean reflectance of the OLI multispectral bands.

Table 1. OIF highest rankings.

Rank	Band Triplet	%
1	7,5,1	72.17
2	7,6,1	72.15
3	7,6,2	71.63
4	7,2,1	71.35
5	7,3,1	70.81
6	7,5,2	70.62

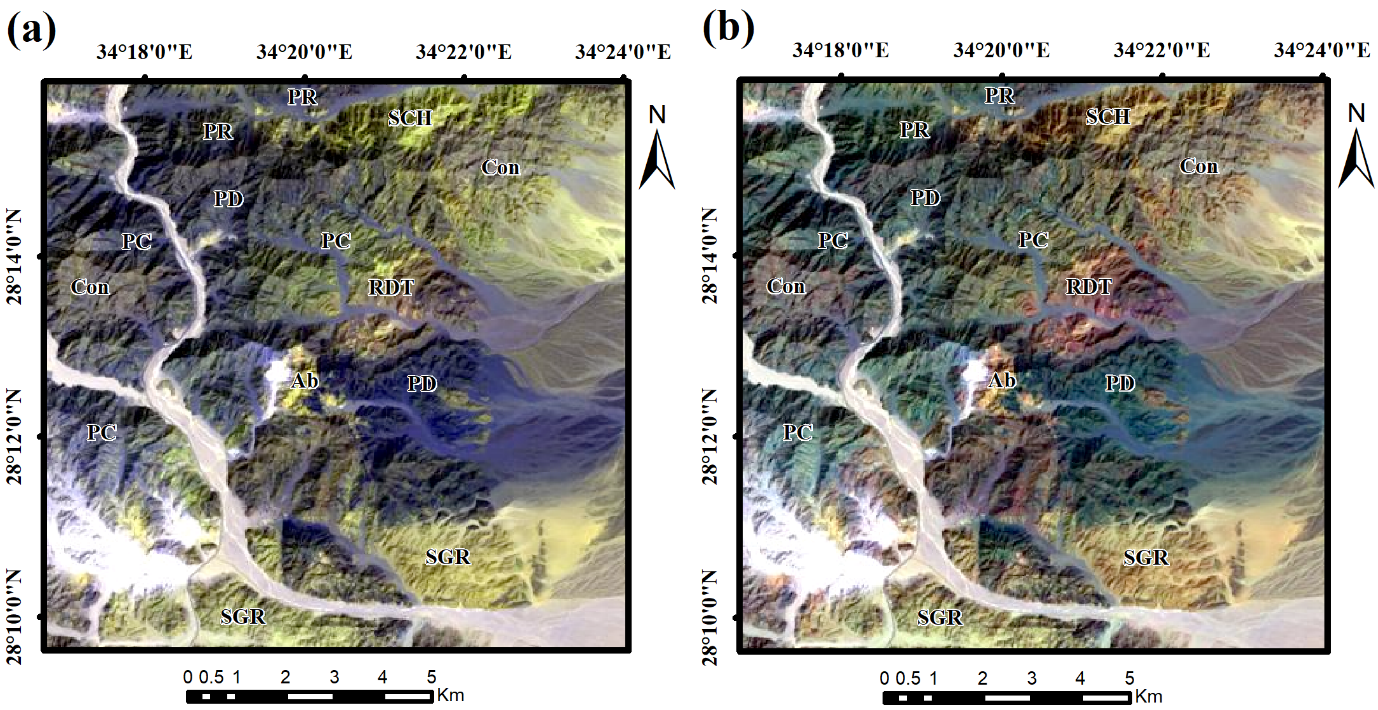

Figure 4. *Cont.*

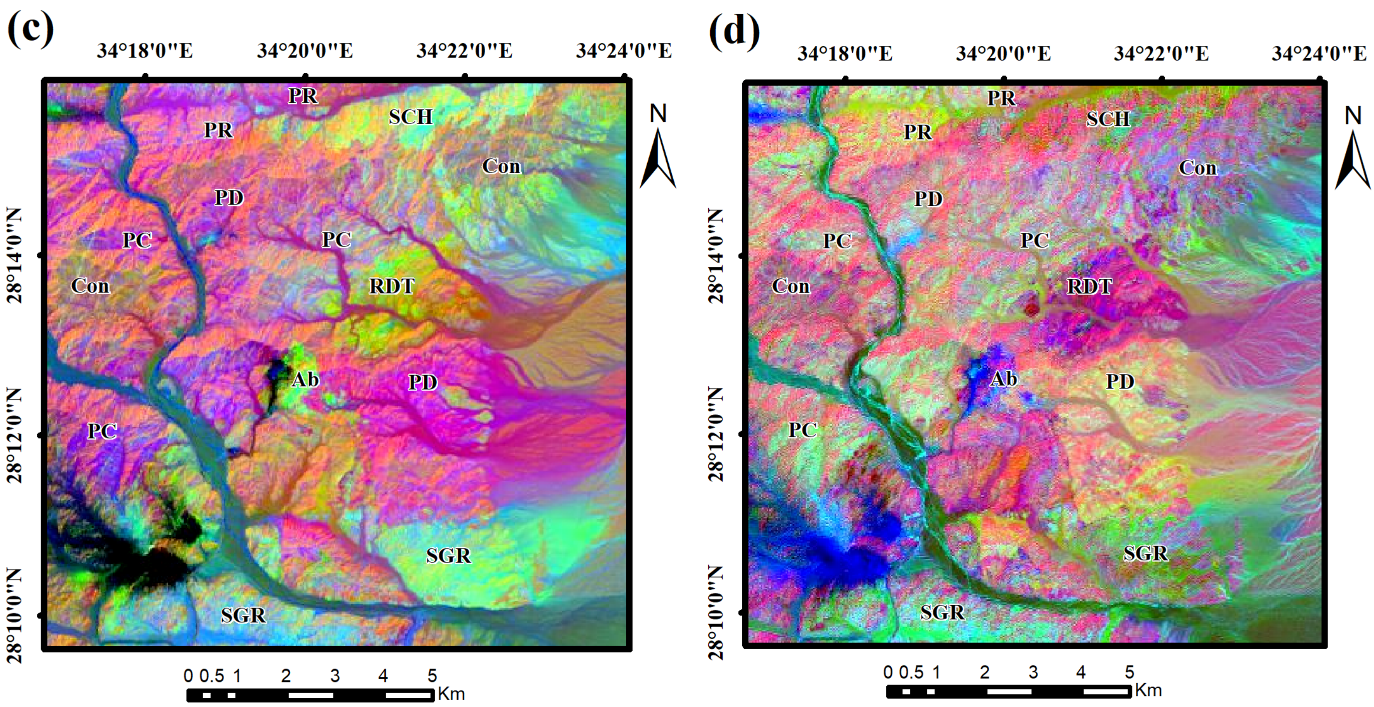

Figure 4. (**a**) Landsat-8 7, 6, and 1 in RGB false color composite. SCH: schist, PR: porphyritic rhyolite, PD: porphyritic dacite, PC: pyroclastic, RDT: rhyodacitic tuffs, Con: conglomerate, SGR: syenogranite, Ab: albitite. (**b**) Landsat-8 7, 5, and 1 in RGB false color composite. (**c**) Landsat-8 PCA (PC1, PC2, and PC3 in RGB). (**d**) Landsat-8 PCA (PC1, PC3, and PC6 in RGB).

4.1.2. Principal Component Analysis (PCA)

Among the many multivariate statistical methods, principal component analysis (PCA) transform is crucial [82,83]. In order to separate noise components and decrease the spectral dimensionality of the data, PCA can be used to produce uncorrelated output bands. Based on the eigenvalues of PCA, the first PCA band contained the highest variance of 96.71%, while the second PCA band contained the second-highest variance of 2.27% (Table 2). The last PCA band contained the minimum variance, high correlation, and noise. In this study, the best PCAs were PC1, PC2, PC3, and PC6 according to the eigenvectors for the OLI bands. Therefore, by projecting the first three principal components, a false color composite was created for PC1, PC2, and PC3 in RGB. Porphyritic rhyolite, porphyritic dacite, and pyroclastic are shown in pink. Syenogranite is characterized by cyan color. The conglomerate shows a pale gray color on the eastern and western sides of the study district. Rhyodacitic tuffs are shown as a yellowish-green color, while albitite shows as a light green color (Figure 4c). Another PCA band composite of the OLI data (PC1, PC3, and PC6) in RGB (Figure 4d) discriminated between lithological rock units in the study district.

Table 2. The eigenvector values of PCA for OLI bands.

Eigenvector	Band 1	Band 2	Band 3	Band 4	Band 5	Band 6	Band 7	Eigenvalues %
PC 1	0.9318	−0.3512	0.08086	−0.0438	0.0002	−0.0004	0.00142	96.71
PC 2	−0.29157	0.8543	−0.4064	−0.1015	0.09809	0.00198	−0.0049	2.27
PC 3	0.19939	−0.2991	0.87965	−0.2182	0.22019	0.02908	−0.0056	0.51
PC 4	−0.025	0.15422	−0.1403	−0.9642	−0.1612	−0.0116	0.01049	0.23
PC 5	−0.0712	−0.16038	−0.1694	−0.0889	−0.75793	0.53086	−0.1187	0.14
PC 6	0.03617	−0.0867	0.07753	−0.04854	−0.5231	0.77822	−0.3218	0.11
PC 7	0.00777	−0.0169	0.0097	0.01441	−0.0748	0.33403	−0.93924	0.03

4.1.3. Minimum Noise Fraction (MNF) Transforms

The MNF lowers the dataset's dimensionality while keeping a sparse number of noise-free components. As a result, less computing power is needed for subsequent processing. The result of this study revealed that the first MNF bands (MNF3, MNF2, MNF1; MNF1, MNF2, MNF4; and MNF2, MNF3, MNF4) in RGB provide premium lithological differentiation because they carry the most information and have less noise than subsequent bands (Figure 5a–c). For example, MNF3, MNF2, and MNF1 in RGB showed good discrimination between different rock units of the study area. This contrast gives exquisite detection of rhyodacitic tuffs (pink color) in the center of the investigated area, while syenogranite shows with a pinkish-yellow color (Figure 5a–c).

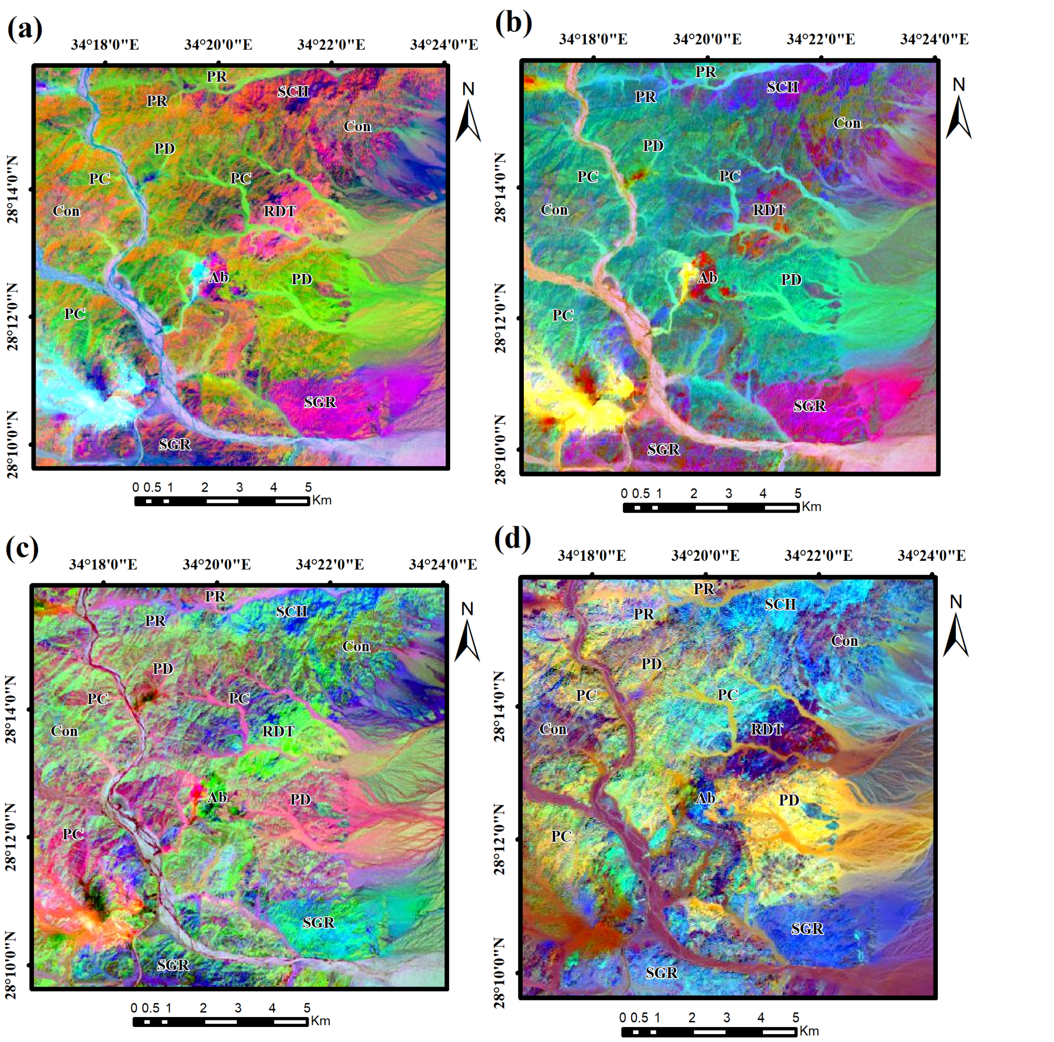

Figure 5. (**a**) Landsat-8 MNFs (MNF3, MNF2, and MNF1 in RGB). (**b**) Landsat-8 MNFs (MNF1, MNF2, and MNF4 in RGB). (**c**) Landsat-8 MNFs (MNF2, MNF3, and MNF4 in RGB). (**d**) OLI RGB color ratio image (4/6, 6/7, and 4/1) for the study area matching with [84]. Symbols as shown in Figure 4.

4.1.4. Band Ratio (BR)

A popular and effective image processing method called band ratio is used to highlight anomalies and enhance the spectral differences between surface materials while suppressing other information, such as changes in scene illumination conditions [84]. Consequently, this technique was utilized in this study to enhance the discrimination between rock units. Regardless of the absolute reflectance values observed in the bands, the ratioed images clearly show the variations in the slopes of the spectral reflectance curves between the two bands in question [85,86]. Several band ratios were used in this study to differentiate between lithological rock units of the Wadi Kid area. The band ratio (4/6, 6/7, and 4/1) shows albitite rocks with blue color, syenogranite with light blue color, schist with pale blue color, and Hammamat conglomerates with a reddish-blue color (Figure 5d) that corresponds to (3/5, 3/1, and 5/7) used in [84]. A new FCC band ratio (2/1, 3/4, and 4/7) was created to discriminate between different rock units in the study area. This FCC was used to detect clearly different types of granitic rocks, where albitite appears with an orange color in the center of the study area, and syenogranite is characterized by a pinkish-red color on the southern side of the investigated area (Figure 6).

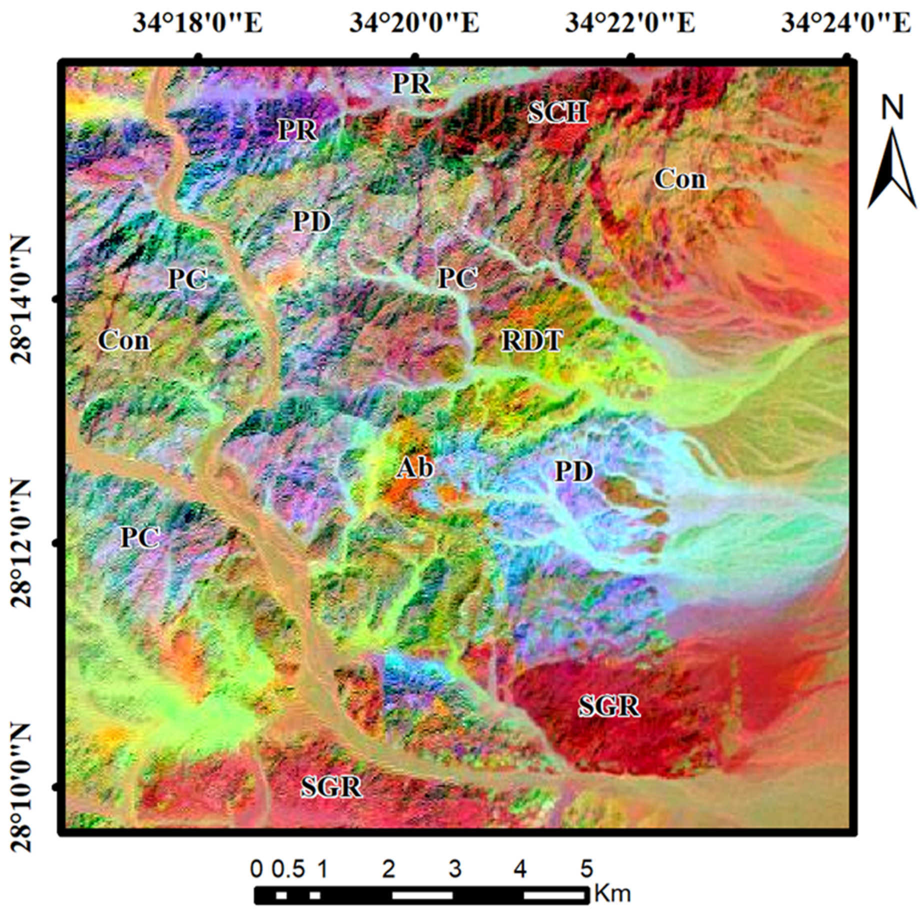

Figure 6. OLI RGB color ratio image (2/1, 3/4, and 4/7) for the study district.

4.2. Fieldwork and Analytical Techniques

4.2.1. Fieldwork

In the Wadi Kid district, the main rock assemblage consists of metasediment sequences, granitic intrusions, and gabbros. These rocks were mainly observed in the Wadi Samra, Khashm El-Fakh, Khashm El-Biya, and Ghorabi El-Hatimyia areas. Metasediments are represented by well-developed foliated fine–medium-grained dark gray schists (Figure 7a–c). The S1 deformational event is characterized by a major scale overturned fold with northwest–southeast axial trends affected by intense deformation and metamorphism (Figure 7a). Metasediments are affected by acidic dykes.

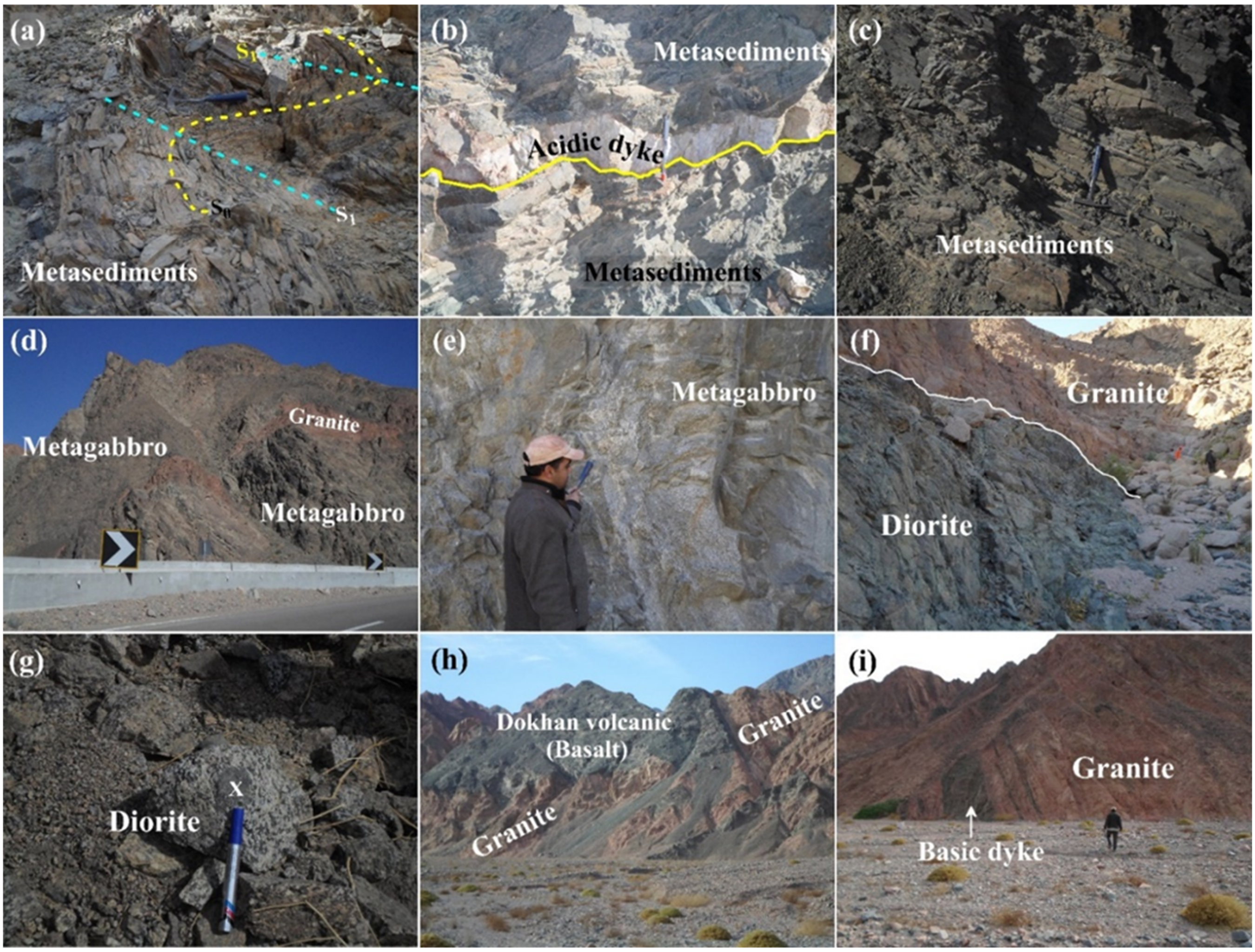

Figure 7. Field photographs showing (**a**) S_0 foliation (delineated by yellow dashed lines) and mesoscopic, tight-folded, overturned (recumbent) metasediments (Schist) at Wadi Tarr; (**b**) acidic dyke cross-cutting metasediments (metagraywackes) at Wadi Ghorabi El-Hatimyia; (**c**) well-developed foliation in schists at Wadi Samra; (**d**) offshoots of granites within Shahira gabbros; (**e**) pegmatoidal gabbros dissecting the gabbros at Wadi Shahira; (**f**) intrusive contact between diorites and granites; (**g**) hand specimen showing a xenolith of mafic rocks embedded in diorites at Wadi Kid; (**h**) offshoots of granites intruding into Dokhan volcanics (basalt) close to east Qabila; (**i**) different basic dykes extruded within granites of the east Qabila area.

The Shahira layered gabbro-diorite is located north of Wadi Kid. Field relations indicate that it is younger than the surrounding metamorphic rocks and older than the post-orogenic granites. This rock is medium–coarse-grained, ranging in color from dark to light greenish-gray (Figure 7d,e). Granitic rocks are intercalated with metagabbro (Figure 7d). Few pegmatitic xenoliths can be observed (Figure 7e). Diorites are characterized as well exposed in Wadi Kid and the east area of Qabila, and close to the contact with the granitic rocks (Figure 7f). Few xenoliths of mafic enclaves are observed within the gabbros near the contacts with the granitic country rocks (Figure 7g).

The younger granites cropping out high-relief masses, as well as exfoliation and weathering, were recorded. The granitic rocks are stained by a red color and in sharp contact with diorites and Dokhan volcanics (Figure 7f–i). These rocks are usually jointed and fractured. The available zircon U-Pb ages of the granitic rocks range from 604 to 607 Ma [51,69,87], which represents the crystallization age of the magma. The albitite masses are isolated from any granitic intrusions and have intrusive contacts against the country rocks, without any structural control. The main body of albitites (≈1.2 km^2) occurs as small and brecciated irregular intrusions encountered upstream of Wadi Tarr (Figure 8a–e). On the other hand, the small albitite masses of Wadi Ghorabi El-Hatimyia and Wadi Khashm El-Fakh have a porphyritic texture defined by a fine-grained matrix carrying large albite phenocrysts with structural rotation and a distinctively volcanic texture.

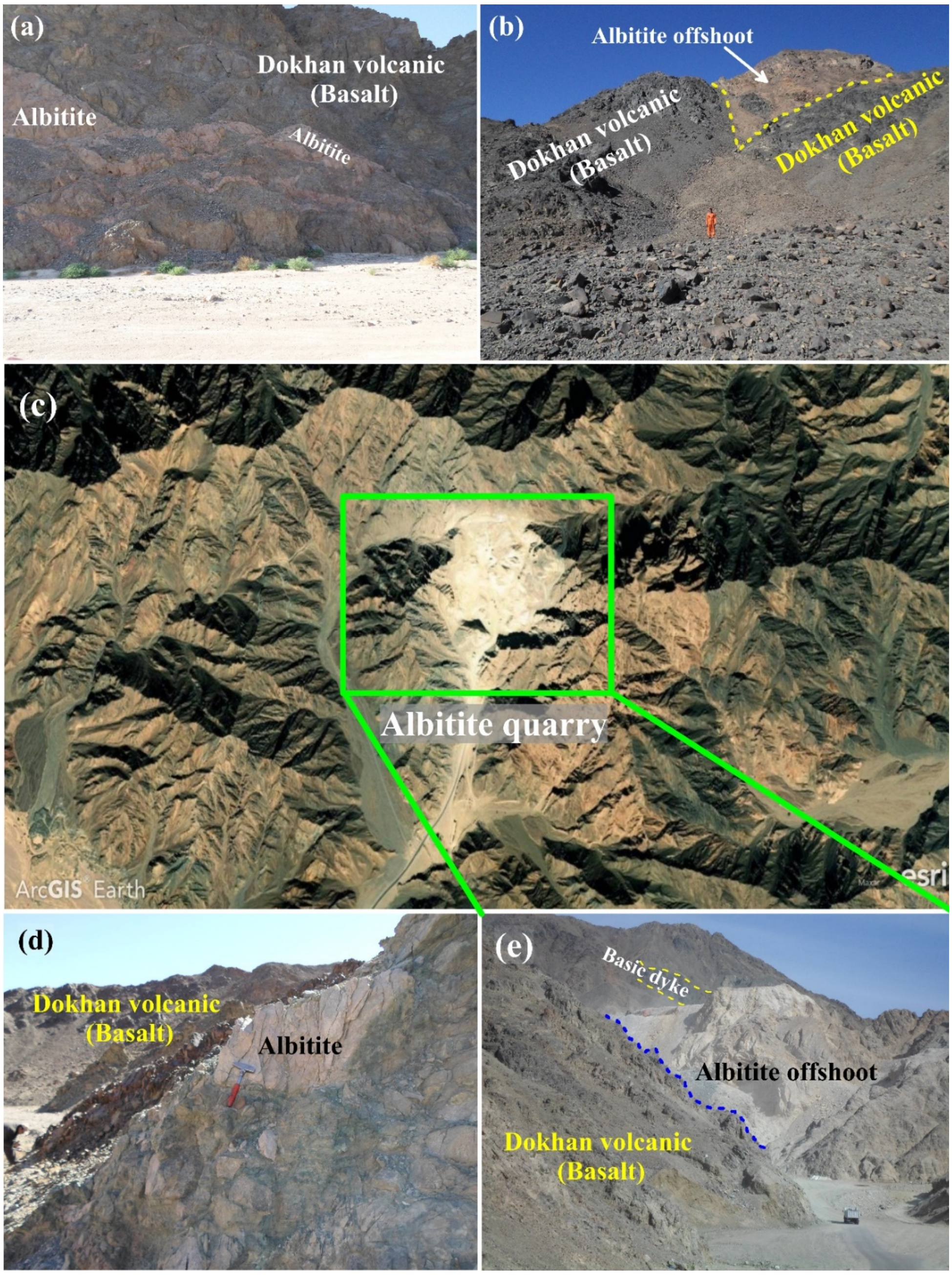

Figure 8. Field photographs showing different localities of albitites: (**a**–**d**) Offshoots of buff-colored albitites cross-cutting Dokhan volcanics (basalt) in Wadi Samra, Wadi Khashm El-Fakh, and Wadi Tarr. (**c**) Google Earth satellite image showing light-colored albitite masses in the Tarr quarry. (**e**) General view showing albitite offshoots in the Tarr quarry.

The Kid Dokhan volcanics have compositions ranging from andesites to rhyolites. The studied dyke's swarms are composed of mafic (trachybasalts–basalts), intermediate (basaltic andesites–trachyandesites), and felsic types (rhyodacites–rhyolites), according to field studies and the previous literature [88]. Both metamorphic and plutonic rocks are crosscut by dykes in the investigated area (Figure 9a,b). The observed dyke rocks are vertical to sub-vertical in shape, unevenly distributed throughout the studied region, and have sharp contacts with the surrounding rocks.

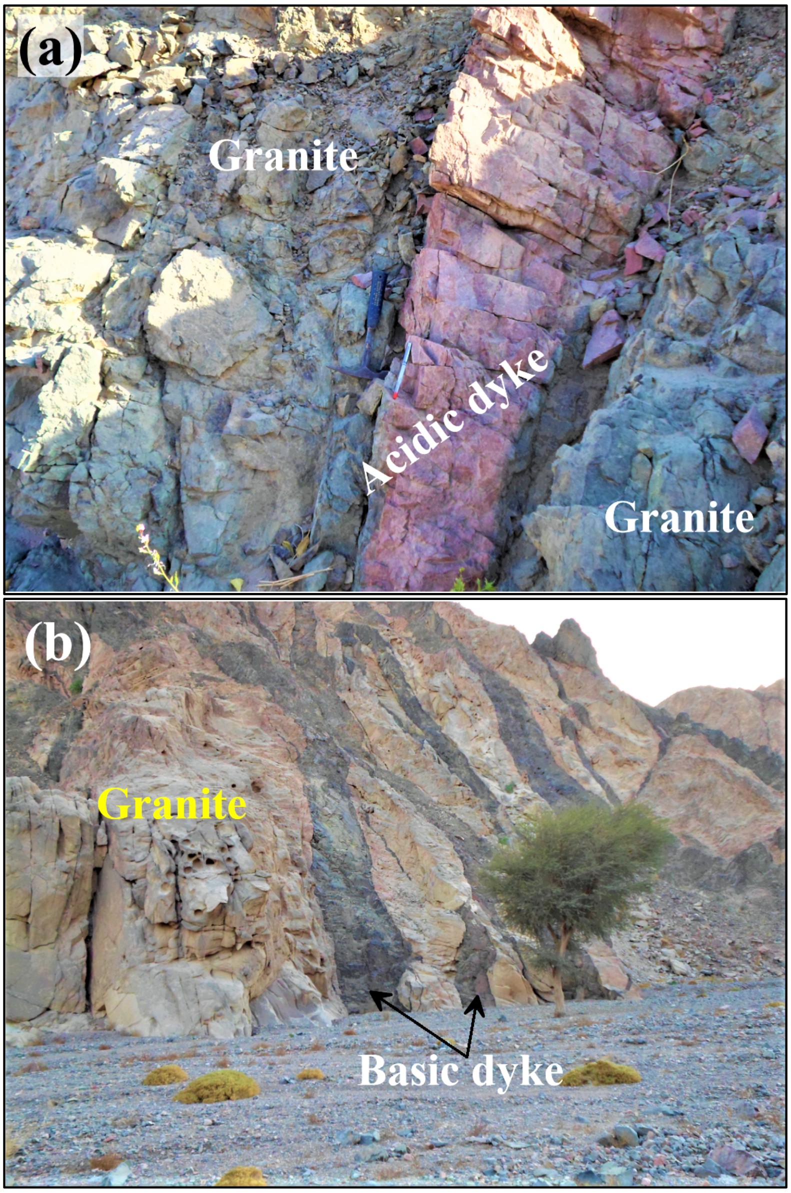

Figure 9. Field photographs showing (**a**) a thick vertical buff/acidic dyke and (**b**) a general view of the different sizes of basic dykes extruded within the younger granites.

4.2.2. Petrographic Studies

The petrographic description of the thin sections representing the different rock units exposed in the studied areas was dealt with. These rock units, arranged chronologically from oldest to youngest, are metasediments, Shahira gabbro, diorites, granitic rocks, albitites (syenites), and aplitic dykes. The metasediments are represented by tremolite–actinolite schists. According to data on the modal composition for the plutonic rocks plotted on the IUGS classification diagram as described in [89] (Figure 10), the plutonic rocks are represented by gabbro, diorites, granitic rocks, and syenite.

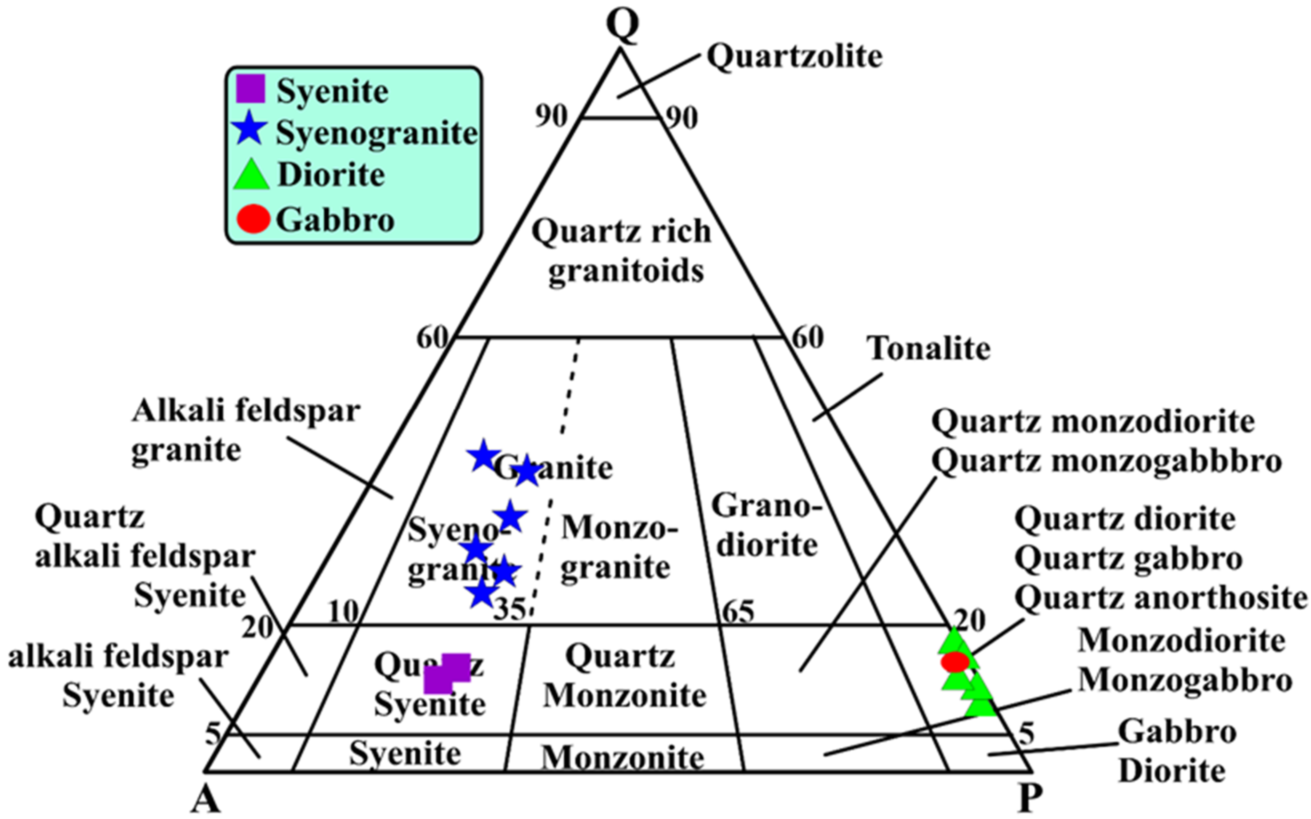

Figure 10. Modal composition of the studied plutonic rocks according to [89].

4.2.3. Metasediment Rocks (Tremolite–Actinolite Schists)

The metasediments are represented by tremolite–actinolite schists. They are characterized by a schistose texture displaying fine–medium-grained rocks. The tremolite–actinolite schists are composed mainly of actinolite, tremolite, and quartz, as well as some accessory minerals such as carbonate and opaque minerals (Figure 11a–d). Tremolite and actinolite occur as fine-grained, acicular, elongate, and prismatic crystals whose orientation imparts the rock with its foliation feature (Figure 11a). They form long prismatic and rhombic crystals that are well oriented with the foliation. Actinolite exhibits a pale green color, usually fibrous in shape and wrapped with tremolite due to deformation (Figure 11b,c). Quartz occurs as colorless, medium–fine-grained, and with a granular shape (Figure 11b,c). Carbonate minerals occur as fine–medium-grained aggregates or patches of colorless, euhedral and subhedral crystals. Occasionally, these carbonates occur as mature and immature granular aggregates (Figure 11d). Opaque minerals occur as interstitial, fine grains disseminated within tremolite and actinolite. They embay fractures of both tremolite and actinolite—mostly black, scattered grains arranged along the schistosity planes (Figure 11b).

4.2.4. Plutonic Rocks

(A) Shahira gabbros

Shahira gabbros display a hypidiomorphic texture, as well as subordinate ophitic, subophitic, and cumulated textures. They consist mainly of hornblende, olivine, pyroxenes, and plagioclase. The main secondary minerals include chlorite and biotite, while the accessory minerals are opaque minerals (Figure 11e–i). Olivine is distinguished by tabular high-relief crystals and altered to fine fibrous pyroxene and iron oxides (Figure 11e). Hornblende and pyroxene occur as subhedral crystals with pale green to pale yellowish-green and green colors (Figure 11h). Both hornblende and pyroxene crystals are altered into chlorite, while others contain opaque minerals (Figure 11e,g).

Plagioclase occurs as deformed or altered prismatic, tabular crystals of saussurite (Figure 11f,h). Quartz occurs as fine–medium-grained euhedral or subhedral crystals and corroded by plagioclase, hornblende, and pyroxene crystals (Figure 11g). Biotite is found as subhedral, brown, elongated flakes that are strongly dichroic. Biotite is partially altered to chlorite (Figure 11i). Opaque minerals occur as fine–medium spots arranged along microfractures and cleavages of minerals.

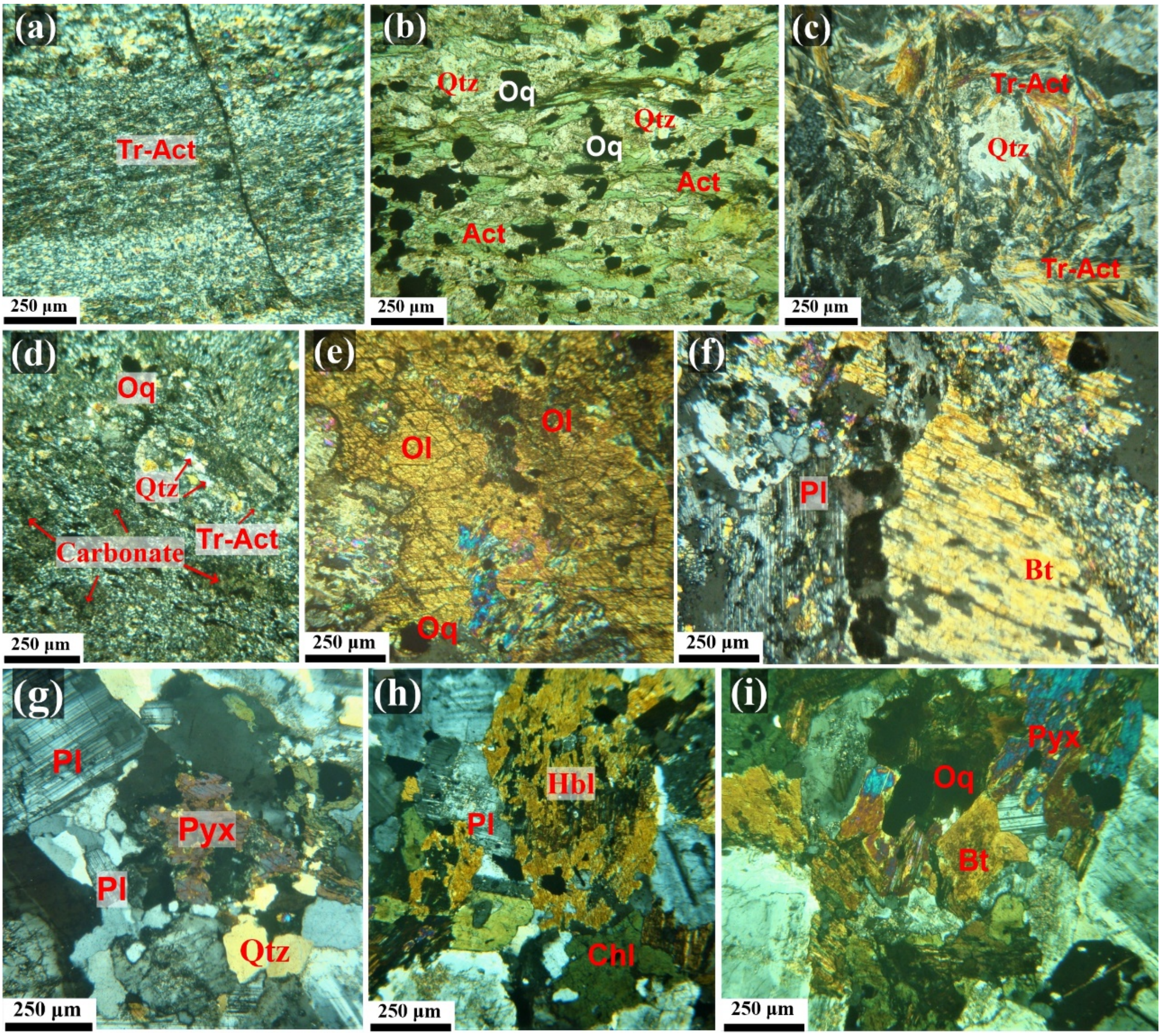

Figure 11. Photographs showing (**a**) well-oriented tremolite–actinolite (Tr-Act) crystals parallel with the foliation; (**b**) green actinolite (Act) crystals associated with quartz (Qtz) and opaque minerals (Oq); (**c**) disordered acicular prismatic tremolite–actinolite (Tr-Act) crystals associated with quartz (Qtz); (**d**) granular texture of quartz (Qtz) associated with tremolite–actinolite and immature carbonate minerals; (**e**) high-relief olivine (Ol) crystals; (**f**) brown biotite (Bt), prismatic with tabular plagioclase (Pl) crystals; (**g**) twinning of plagioclase (Pl) with clear quartz (Qtz) and pyroxene (Pyx) crystals; (**h**) hornblende (Hbl) containing opaque minerals (Oq) with plagioclase (Pl) crystals; (**i**) brown biotite (Bt) flakes associated with pyroxene (Pyx) crystals.

(B) Diorites

Diorites are primarily composed of plagioclase, quartz, hornblende, and pyroxene, so they have a medium–coarse-grained texture. The three main secondary minerals are saussurite, chlorite, and zoisite. The two primary accessory minerals are opaque and carbonate minerals. The texture of the rock is granular, showing as tabular subhedral–anhedral crystals of plagioclase. In addition to their alteration into sericite and zoisite, they occasionally disappear and exhibit lamellar twinning (Figure 12a). Quartz occurs as medium-grained, subhedral–euhedral crystals. Sometimes, micro quartz crystals show shadow extinction filling the interstitial spaces (Figure 12b). Hornblende occurs as subhedral crystals and is mostly altered to chlorite (Figure 12c). These crystals generally contain opaque minerals as inclusions.

Pyroxene occurs as subhedral crystals that are highly altered to chlorite (Figure 12d). Saussurite forms thin tabular crystals and shreds that present as fine flakes, with minute inclusions within the plagioclase as an alteration product (Figure 12d). Zoisite is formed from the alteration of plagioclase crystals (Figure 12b). Carbonate minerals occur as fine-to-very-fine grain aggregates or patches of colorless, euhedral–subhedral crystals. Chlorite exists as fine–medium grains dispersed in the interstitial spaces (Figure 12,e). Opaque minerals are fine–coarse-grained and occur as disseminated fine dots within the mineral constituents (Figure 12e,f).

(C) Syenogranites

Syenogranites are medium–coarse-grained and display a porphyritic texture consisting of quartz, plagioclase, potassic feldspar, and biotite. Accessory minerals are represented by opaque minerals. On the other hand, chlorite, muscovite, and kaolinite are the main secondary minerals (Figure 12g–j). Plagioclase consists of subhedral tabular crystals. Some plagioclase laths display microperthites (Figure 12g). Microcline is a representative of potassic feldspars. Microcline shows subhedral crystals and frequently offers an anti-perthite texture (Figure 12j). Potassic feldspar can occasionally be altered to kaolinite and filled with quartz. Plagioclase and microcline are mainly associated with one another (Figure 12h). Compared to euhedral crystals, quartz crystals are less abundant and subhedral. In Figure 11i, they exhibit significant undulose extinction. Biotite consists of anhedral–subhedral elongated flakes. Some biotite is altered into chlorite (Figure 12i). Muscovite occurs as subhedral crystals filing the interstitial spaces (Figure 12h).

(D) Albitites

Albitites are medium–coarse-grained with a porphyritic texture and composed of plagioclase laths, quartz, and opaque minerals. Alkali feldspar occurs as subhedral–anhedral crystals, represented mainly by albite composition. Plagioclase feldspars are surrounded by quartz aggregates (Figure 12k). Quartz is present as subhedral–anhedral crystals. Some quartz crystals occur as inclusions in plagioclase crystals, producing a myrmekitic texture. Opaque minerals characterized by a dark brownish-black color and occur as inclusions in the feldspar and quartz (Figure 12k).

The aplitic dykes are mostly composed of quartz crystals, with slight amounts of feldspars, and sometimes a few flakes of mica, such as muscovite. These dykes are fine-to very-fine-grained (Figure 12l). Quartz is predominantly of a milky-white variety, but yellowish quartz may also occur. It occurs as fine-to-very-fine, subhedral–euhedral, water-clear crystals, in two generations. These crystals possess low relief, strong wavy extinction, and corrosive action with the surrounding feldspar crystals (Figure 12l). They form mosaic-like aggregates and are either completely free of inclusions or may contain extremely opaque minerals and muscovite (Figure 12l).

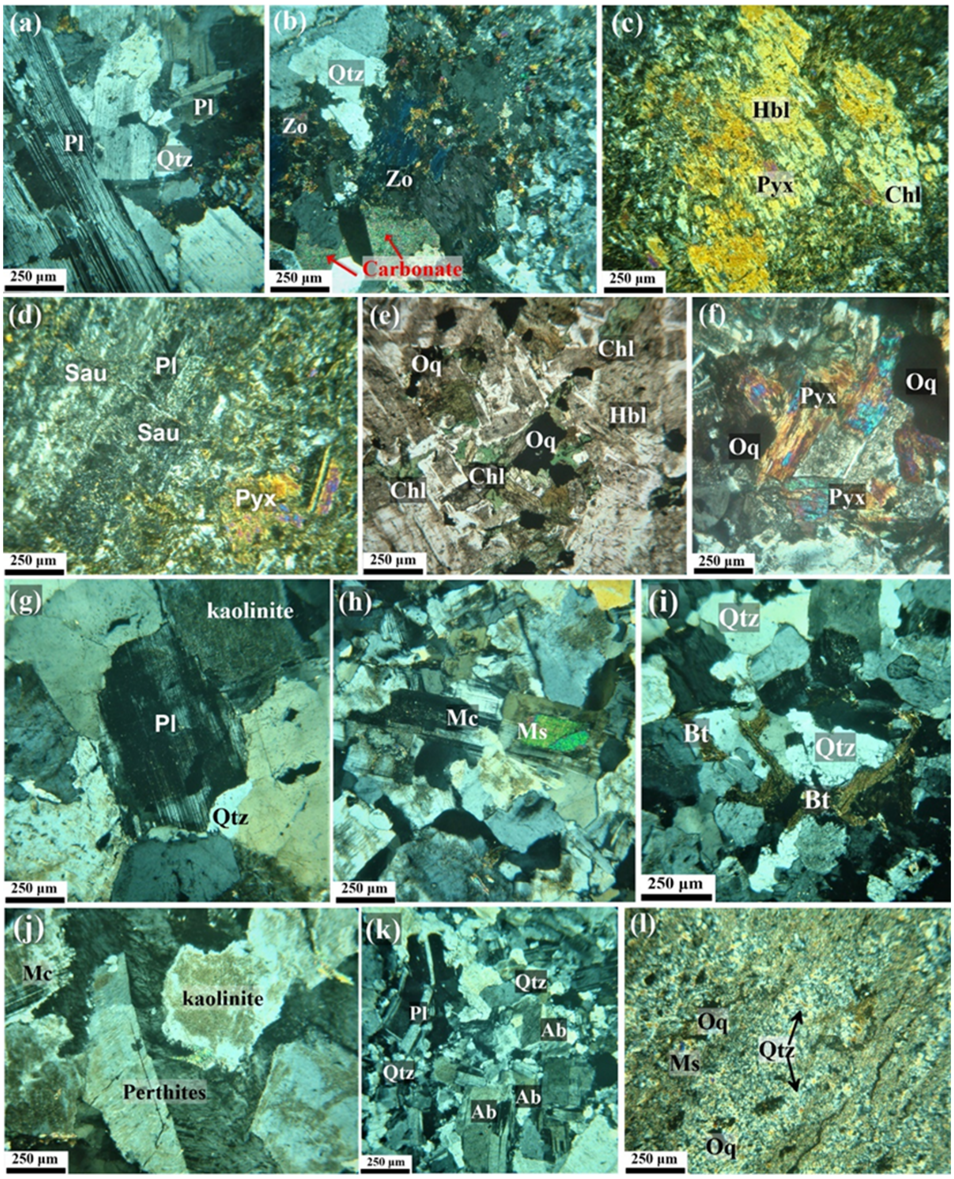

Figure 12. Photographs showing (**a**) pericline lamellar twinning of tabular plagioclase (Pl) crystals associated with quartz (Qtz); (**b**) Berlin blue zoisite (Zo) crystals after plagioclase (Pl) accompanied by immature carbonate minerals; (**c**) elongated hornblende (Hbl) prismatic crystals containing inclusions of pyroxene (Pyx) altered to chlorite (Chl); (**d**) tabular plagioclase (Pl) crystals altered to saussurite (Sau) associated with pyroxene (Pyx) crystals; (**e**) high-relief and dark green chlorite (Chl) crystals associated with opaque minerals (Oq); (**f**) pyroxene (Pyx) crystals exhibiting high-interference colors associated with opaque minerals; (**g**) plagioclase (Pl) crystals altered to kaolinite; (**h**) microcline (Mc) and quartz crystals associated with muscovite (Ms) enclosed within the feldspars; (**i**) scattered biotite (Bt) flakes partially altered to chlorite; (**j**) Large perthite crystals associated with kaolinitized feldspars; (k) albite plagioclase (Ab-Pl) crystals and quartz (Qtz) in albitite (syenite) rocks; (**l**) quartz (Qtz) revealing undulose extinction and opaque minerals (Oq) enclosed within aplitic dykes.

4.3. Geochemical Studies

4.3.1. Metasediments

(a) Major and Trace Elements

Table 3 shows the studied rocks' major and trace elemental composition, distinguished by low-to-high SiO_2 contents, with values ranging between 47.63 and 65.51 wt.%. The Al_2O_3 (16.46–21.14 wt.%), CaO (1.28–9.25 wt.%), and MgO (0.7–12.99 wt.%) contents are medium–high, while the Fe_2O_3 (0.39–4.64 wt.%) and TiO_2 (0.2–0.1.5 wt.%) contents are very low. Alkaline minerals (4.08 < $Na_2O + K_2O$ < 9.46 wt.%) are relatively low to medium in content. The K_2O/Na_2O ratio of this rock is very high (0.02–0.59), which suggests a very poor detrital feldspathic charge. The contents of other oxides, such as Cr_2O_3 (0.004–0.054 wt.%), MnO (0.01–0.17 wt.%), and P_2O_5 (0.24–0.79 wt.%), are very low (less than 1).

Table 3. Whole-rock major oxides and trace element compositions of Wadi Kid metasediments.

Rock Type	Metasediments				
Sa. No.	**4T**	**14 Kh**	**2 Sam**	**9 Kh**	**1 Gh**
			Major oxides (wt.%)		
SiO_2	65.517	52.058	60.792	47.632	58.973
TiO_2	0.326	0.288	0.928	1.564	0.904
Al_2O_3	21.147	17.423	16.499	17.685	20.254
FeO	0.318	2.868	0.958	8.258	3.413
Fe_2O_3	0.394	1.906	0.944	4.643	3.364
MnO	0.011	0.175	0.034	0.177	0.035
MgO	0.766	12.995	6.261	5.546	2.54
CaO	1.287	6.615	4.837	9.257	1.896
Na_2O	9.243	4.395	7.491	2.562	6.736
K_2O	0.225	0.632	0.272	1.523	1.386
P_2O_5	0.477	0.247	0.777	0.796	0.278
SO_3	0.068	0.144	0.044	0.024	0.031
Cl	0.031	0.075	0.049	0.027	0.053
Total	**100**	**100**	**100**	**100**	**100**
			Trace elements (ppb)		
Zn	0	9	0	20	5
Sr	30	43	11	99	17
Ba	30	22	50	44	16
Co	-	30	20	25	14
Cr	-	-	27	17	16
Cu	80	20	6	16	5
Y	6	3	7	4	4
Zr	66	63	30	38	23
Nb	3	2	2	3	4
Sr	30	43	11	99	17
Ba	90	22	80	44	16
Ce	-	-	-	38	19
Ga	3	-	4	2	2
Pb	2	-	-	-	-
SiO_2/Al_2O_3	0.491	0.475	0.566	0.430	0.464
Fe_2O_3/K_2O	0.243	0.479	0.540	0.484	0.385
K_2O/Na_2O	0.024	0.144	0.036	0.594	0.206
$CaO+Na_2O$	10.530	11.010	12.328	11.819	8.632
SiO_2/Al_2O_3	0.491	0.475	0.566	0.430	0.464

When compared to the international standards (PAAS, NASC, and UCC), all of these metasediments have high MgO contents and low SiO_2, Fe_2O_3, and CaO contents. The high MgO contents could evoke the nature of their igneous protolith. The rocks show similar contents of Al_2O_3 (average = 18 wt.%), with the international reference suggesting a low clay content. However, the average abundances of the other major motifs are somewhat comparable to the reference constructs reported in Table 3.

(b) Geochemical Origin of the Metasediments

Whole-rock geochemical data of fresh representative rock samples of the metasediments are given in Table 3. The Na_2O-FeO + MgO-K_2O ternary diagram was used in [90] to identify the source of the metasediment materials. The studied metasediments were plotted in the field of graywackes (Figure 13a). This is also supported by the (SiO_2/Al_2O_3)–

(K_2O/Na_2O) binary diagram in [91], where the studied sample fell within the field of pelitic graywackes (Figure 13b), supporting a sedimentary origin. The FeOt-MgO-Al_2O_3 ternary diagram in [92] supports the metamorphic origin of these rocks (Figure 13c). Based on the log (FeO/K_2O) versus log (SiO_2/Al_2O_3) of [93], the sample points show that the metasediments are originally from shales (Figure 13d).

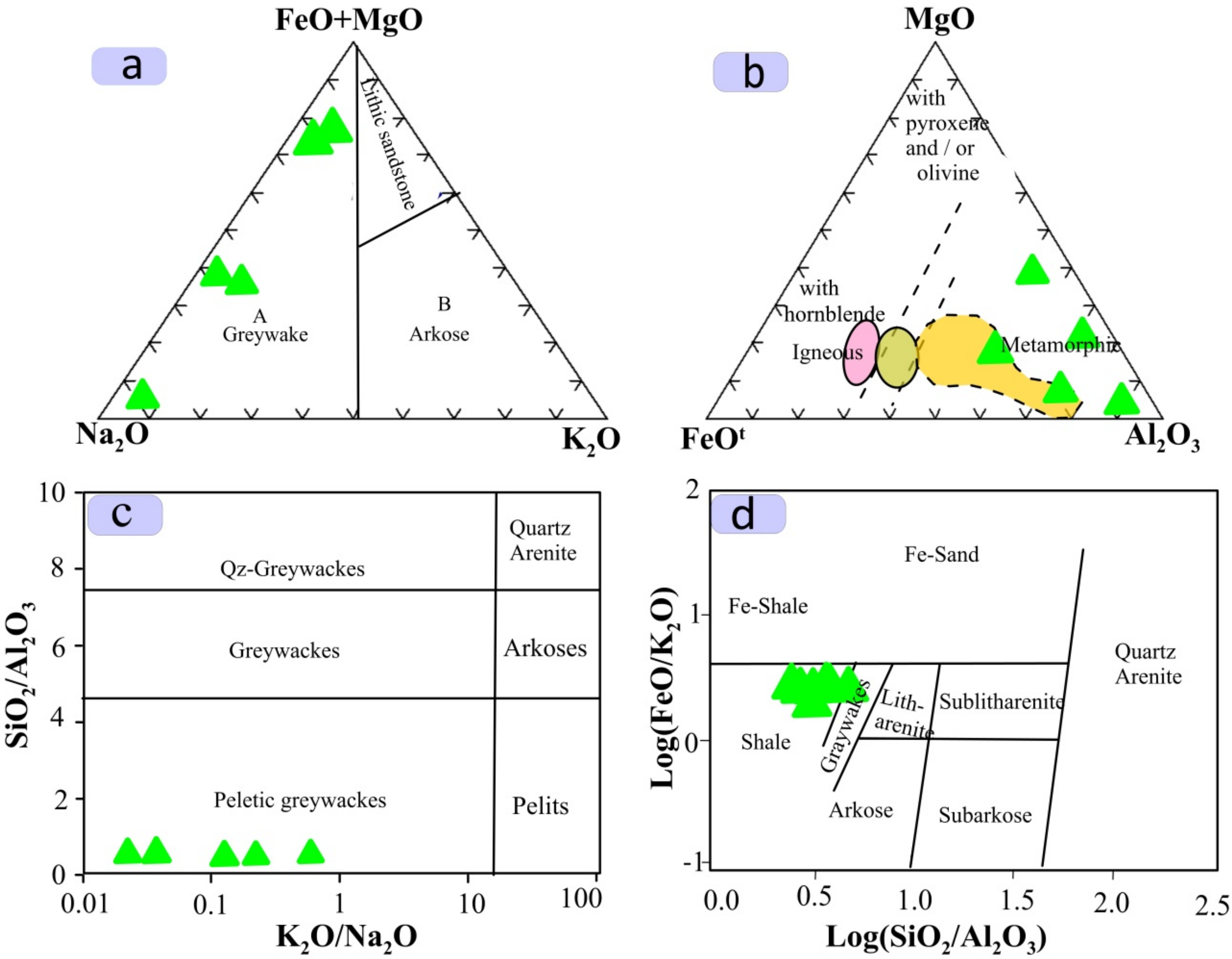

Figure 13. (**a**) Geochemical classification of the metasediments by using the Na_2O-FeO + MgO-K_2O ternary diagram [90]. (**b**) FeO^t-MgO-Al_2O_3 ternary diagram from [91]. (**c**) SiO_2/Al_2O_3 versus K_2O/Na_2O binary diagram [92]. (**d**) Log (FeO/K_2O) versus log (SiO_2/Al_2O_3) binary diagram [93–96].

(c) Harker Diagrams

Harker graphs demonstrate variations in the metasediments' major elemental geochemistry (Figure 14). Overall, the diagram shows negative correlations with Fe_2O_3, CaO, K_2O, and TiO_2. All of the metasediments show a peraluminous character with an $Al_2O_3/(CaO+Na_2O+K_2O)$ ratio higher than 1 (1.30–2.02).

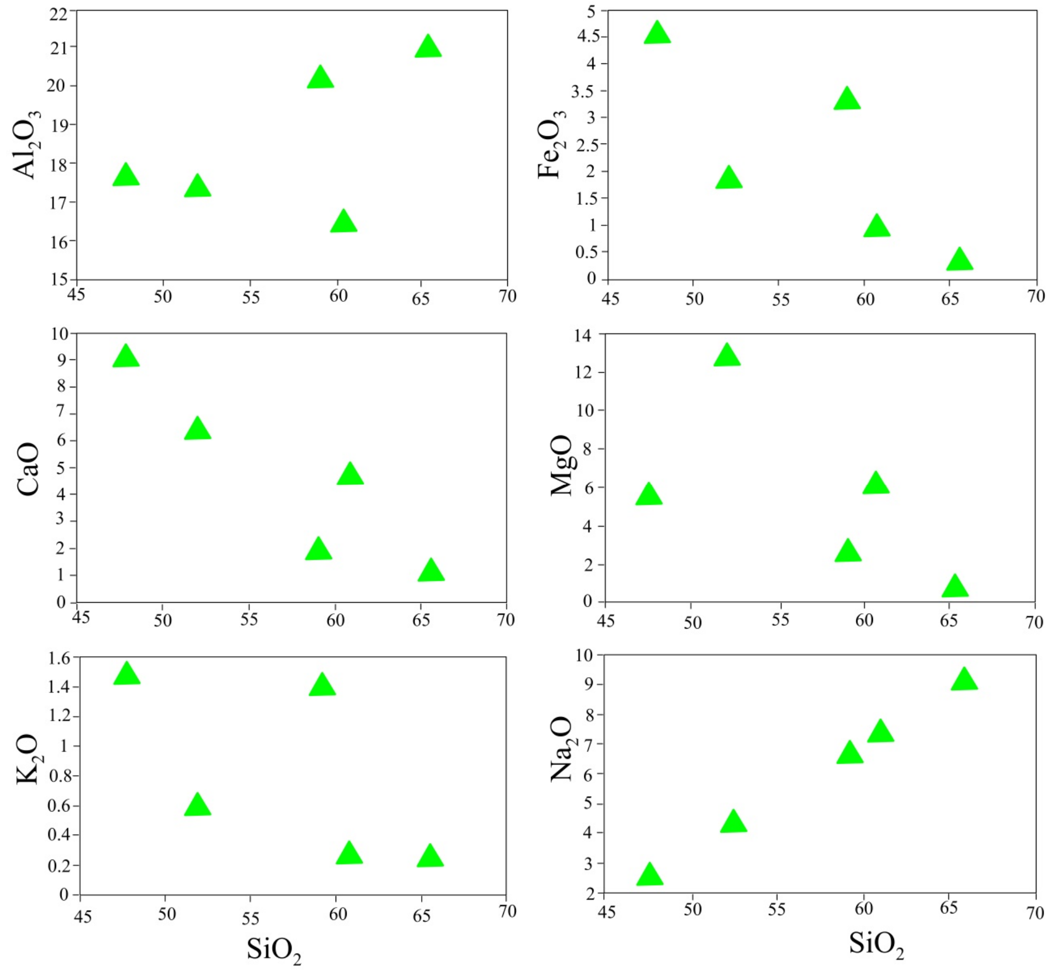

Figure 14. Harker graphs for the Wadi Kid metasediments.

4.3.2. Intrusive Rocks

(a) Classification and Magma Type

Chemically, using the R1-R2 plot from [94] shows that samples of the alkaline rocks are classified as albitite, while the calc-alkaline series samples vary from monzodiorites to granites in composition (Figure 15). The granite samples show high contents of SiO_2 (66.91–72.74 wt.%) and $Na_2O + K_2O$ (8.78–10.15 wt.%). These samples display low CaO (0.88–1.6 wt.%), MgO (<1.85 wt.% in most samples), and Fe_2O_3t (<4 wt.%) contents, typical of granites sensu stricto and similar granites of south Sinai [95].

The monzodiorite samples are characterized by low SiO_2 (54.19–57.29 wt.%) and high CaO contents (4.82–9.95 wt.%) compared to granites. The total alkali silica content is variable ($Na_2O + K_2O$: 5.08–6.72 wt.%), and their MgO content varies from 2.45 wt.% to 5.91 wt.%, with high $Mg^{\#}$ values (57.37–71.28) close to the mantle [97]. The alkaline samples show a syenitic composition with variable SiO_2 content (64.86–65.82 wt.%), typical of intermediate rocks. The rocks exhibit high contents of Al_2O_3 and Na_2O (up to 20 wt.% and 10 wt.%, respectively). The MgO content is very low but displays $Mg^{\#}$ between 68.81 and 85.01, indicating rocks derived from the mantle. The $Na_2O + K_2O$ value is up to 10 wt.% for both samples. They display a low K_2O/Na_2O ratio (less than 0.1).

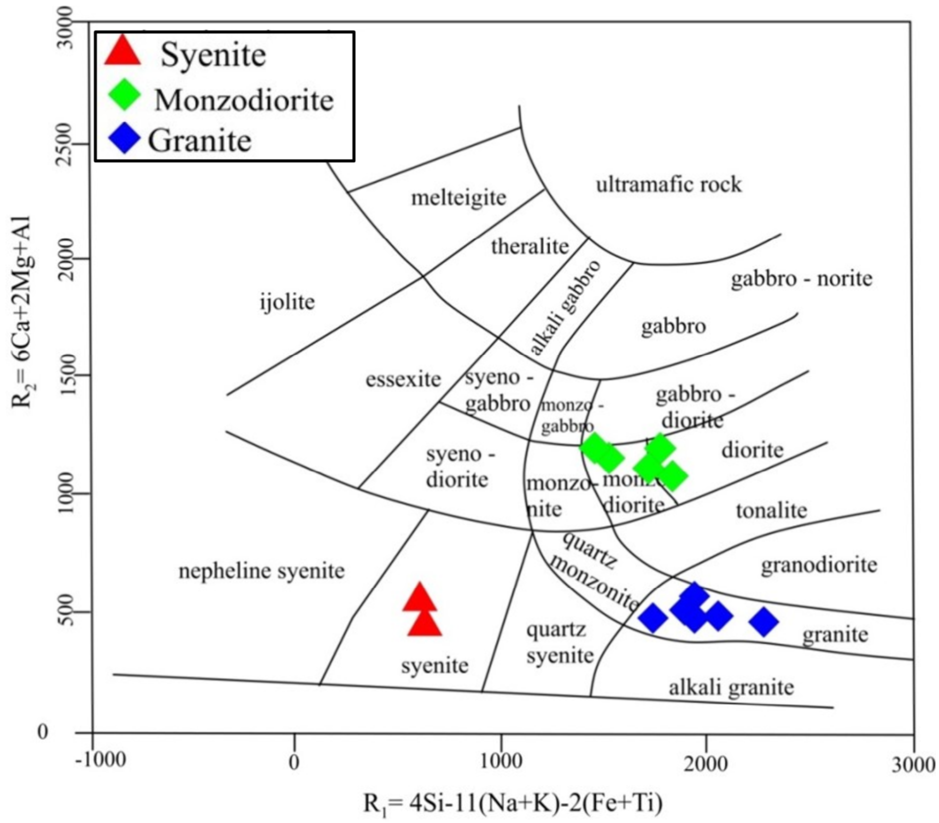

Figure 15. Classification of the studied granites using an R_1-R_2 diagram [94].

In comparison with calc-alkaline rocks in the Sinai Peninsula [39], the Wadi Qabiliya calc-alkaline rocks depict low average SiO_2, Fe_2O_3, and CaO contents, and similar average Al_2O_3 and MgO contents. However, except for the low SiO_2 content in the study district, the other elements are similar to those found in southern Sinai. The alkaline samples in the study district display low SiO_2 and Fe_2O_3 contents compared to alkaline rocks of the Sinai Peninsula. However, they display higher contents of Al_2O_3 and Na_2O than in the Sinai Peninsula. On the Harker diagrams (Figure 15), the three granitic suites display the evolution of major oxides against SiO_2 contents. Apart from total alkalis (K_2O + Na_2O), showing a positive trend, the other compounds (CaO, MgO, TiO_2, and Al_2O_3) display an overall negative correlation when SiO_2 increases (Figure 15). However, it is noticeable that in all diagrams there is a tendency towards broad scattering of data points rather than tight linear trends. In spite of this scattering, all of the general trends of the major oxides are in accordance with a fractional crystallization model, as described by [39] in the Yahmid-Um Adawi district.

Geochemical data on the major oxides and trace elements of Wadi Qabiliya are presented in Table 4. The total alkalis–silica diagram (Figure 16a) of these rocks shows that they are plotted in alkaline and subalkaline fields. On the K_2O versus SiO_2 binary diagram from [96], the subalkaline granites are high-K, calc-alkaline–shoshonite series (Figure 16b).

Table 4. Whole-rock major oxides and trace element compositions of Wadi Kid intrusive rocks.

Rock Type	**Diorite**					**Granite**						**Albitite**	
S. No.	**30 Qe**	**26 Qe**	**2KD**	**7 Qe**	**1 Qe**	**15 Qe**	**21 Qe**	**1KD**	**18 Qe**	**2KF**	**35 Qe**	**13 Kh**	**1T**
Major oxides (wt.%)													
SiO_2	55.335	55.052	57.538	54.191	57.298	69.825	70.059	67.023	69.365	72.741	66.917	64.861	65.828
TiO_2	1.215	1.255	0.511	1.503	1.263	0.279	0.132	0.669	0.223	0.172	0.546	0.93	0.32
Al_2O_3	17.307	16.499	17.947	14.969	15.38	16.46	16.814	15.869	17.427	15.441	15.04	20.562	20.872
FeO	5.264	5.852	2.140	5.815	4.244	0.825	0.429	1.698	0.562	0.444	2.121	0.307	0.206
Fe_2O_3	3.722	4.362	1.820	4.433	3.362	1.053	0.611	2.032	0.765	0.598	2.539	0.411	0.285
MnO	0.19	0.21	0.125	0.13	0.127	0.047	0.048	0.107	0.026	0.088	0.114	0.008	0.165
MgO	4.748	4.42	2.45	5.833	5.911	0.715	0.333	1.857	0.45	0.426	1.173	0.977	0.256
CaO	6.188	5.806	9.958	5.576	4.821	1.298	1.187	1.353	0.943	0.886	1.635	0.866	0.379
Na_2O	2.804	3.369	5.992	2.628	2.827	3.55	4.61	3.153	4.182	3.543	3.261	10.282	10.264
K_2O	2.277	2.35	0.734	3.508	3.142	5.418	5.545	5.634	5.582	5.481	5.551	0.179	0.367
P_2O_5	0.521	0.41	0.225	0.628	0.56	0.125	0.044	0.271	0.112	0.043	0.271	0.46	0.052
SO_3	0.047	0.095	0.149	0.146	0.315	0.064	0.005	0.032	0.047	0.022	0.419	0.038	0.019
Cl	0.028	0.03	0.064	0.121	0.383	0.056	0.016	0.06	0.058	0.027	0.081	0.049	0.056
Total	**100**	**100**	**100**	**100**	**100**	**100**	**100**	**100**	**100**	**100**	**100**	**100**	**100**
Trace elements (ppb)													
Zn	16	17	15	0	10	6	0	11	7	0	0	3	-
Sr	103	82	24	97	199	115	44	27	76	8	97	12	15
Ba	75	53	76	103	15	104	65	75	94	12	103	30	40
Co	18	23	10	20	30	20	10	10	20	20	20	20	-
Cr	-	-	-	26	-	7	-	-	-	-	26	12	-
Cu	11	10	5	9	10	5	10	4	8	3	9	4	4
Y	3	4	9	5	6	4	3	9	1	3	5	6	2
Zr	43	38	88	65	87	16	20	63	28	24	65	25	51
Nb	1	1	7	3	3	2	2	5	1	3	3	4	5
Sr	103	82	24	97	199	115	44	27	76	8	97	12	15
Ba	75	53	76	103	15	104	65	75	94	12	103	39	30
Ce	51	45	44	71	-	0	0	-	0	-	71		-
Ga	4	4	5	3	4	4	5	3	5	2	3	3	4
Pb	3	0	6	3	4	4	4	2	9	6	3	3	2
Na_2O+K_2O	5.081	5.719	6.726	6.136	5.969	8.968	10.155	8.787	9.764	9.024	8.812	10.461	10.631
Mg	61.653	57.380	67.115	64.134	71.285	60.698	58.057	66.097	58.782	63.111	49.647	85.018	68.893
K_2O/Na_2O	0.812	0.698	0.122	1.335	1.111	1.526	1.203	1.787	1.335	1.547	1.702	0.017	0.036

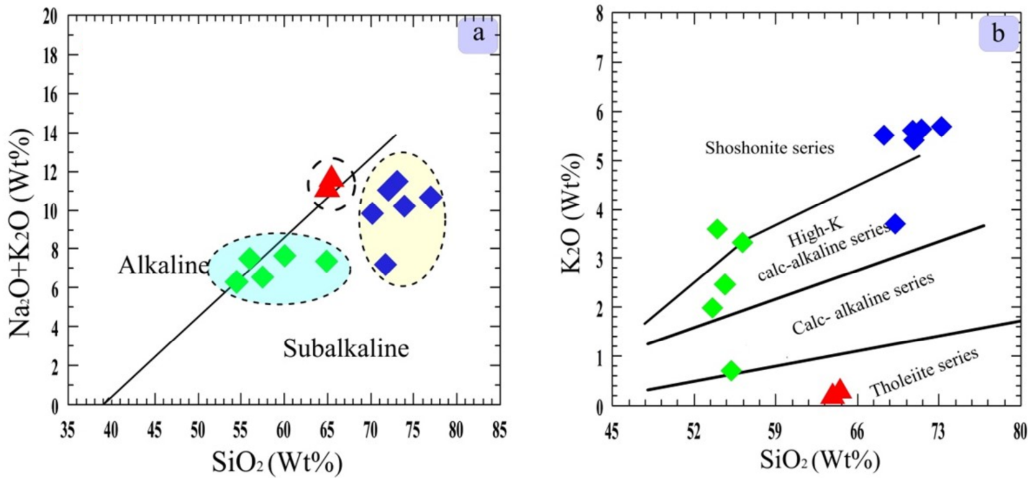

Figure 16. (**a**) Silica (wt.%) versus Na_2O + K_2O [94] and (**b**) Silica (wt.%) versus K_2O (wt.%) [96].

(b) Harker Diagrams

In the SiO_2 vs. oxides Harker diagrams, the distribution of symbols representing different petrographic rocks is virtually linear and scattered. The inter-pluton fluctuations or crustal contamination during magma storage and ascent may be responsible for the general scattering on major elemental Harker diagrams (Figure 17).

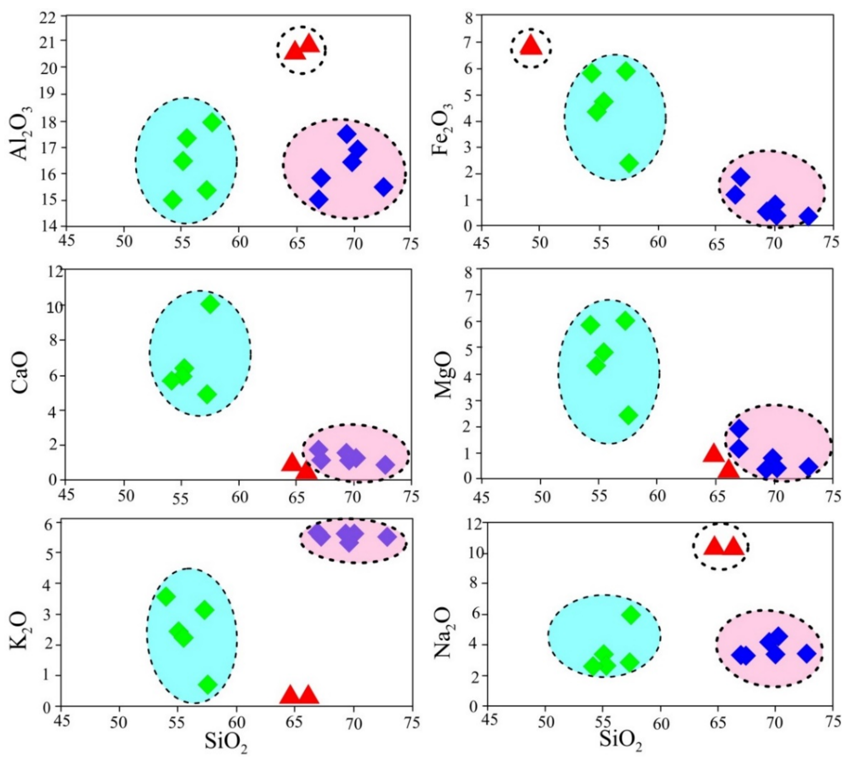

Figure 17. Selected silica (wt.%) versus major elements (wt.%) diagrams for Wadi Kid granites.

(c) Tectonic Environment

All of the calc-alkaline and alkaline samples are magnesian in character on the FeO*/FeO* + MgO vs. SiO_2 diagram (Figure 18a) from [98]. On the Shand's index plot [99], granites and albitite (syenites) are peraluminous, while the monzodiorite samples are metaluminous (Figure 18b). The granites and syenites are I-to-S-type granitoids while the monzodiorites are typical I-type granitoids (Figure 18b). According to [100], the granitic rocks were classified based on their intrusive settings into four main groups: ocean-ridge granites (ORGs), volcanic-arc granites (VAGs), within-plate granites (WPGs), and syn-collision granites (Syn-COLGs). They also suggested that the post-collision granite may be plotted in the volcanic-arc, within-plate, or syn-collision fields depending on the relative proportions of mantle- and crust-derived magmas.

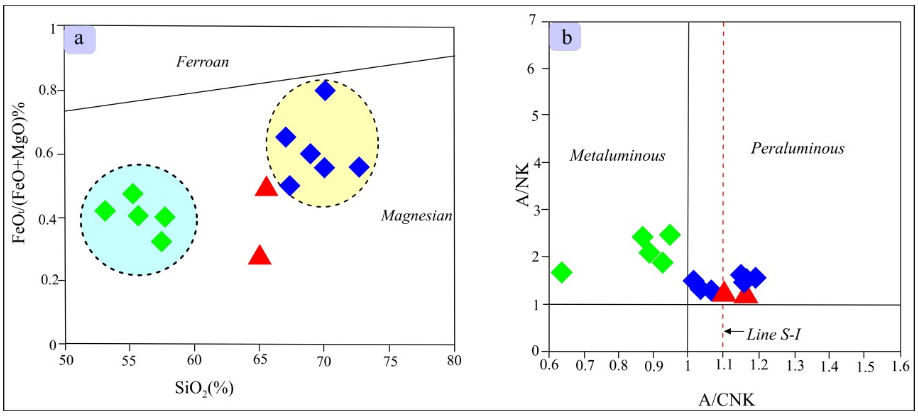

Figure 18. (**a**) Silica (wt.%) vs. FeO/(FeO + MgO) [98] and (**b**) Shand's index molar $Al_2O_3/(CaO + Na_2O + K_2O)$ vs. $Al_2O_3/(Na_2O + K_2O)$ diagram [99].

The analyzed samples have specific trace-element features that are similar to those of within-plate granite (WPG) and some of the syn-collision granite (syn-COLG) fields in the tectonomagmatic differentiation diagrams from [100] (Figure 19). The author recommended interpreting this as a post-subduction extensional occurrence. Both granitic suites have variable trace elements. They display high contents of Ba, Zr, Sr, and Co, along with low Pb and Y, pointing to their felsic compositions. The Y/Nb ratios of both suites of granites vary between 0.4 and 4, with an average of 1.66 (Table 3). The values less than 1.2 characterize mantle-derived granites, while those above 1.2 are typical of crust-derived granites [39,101]. Hence, all samples are most likely derived from the mantle, with crustal contamination.

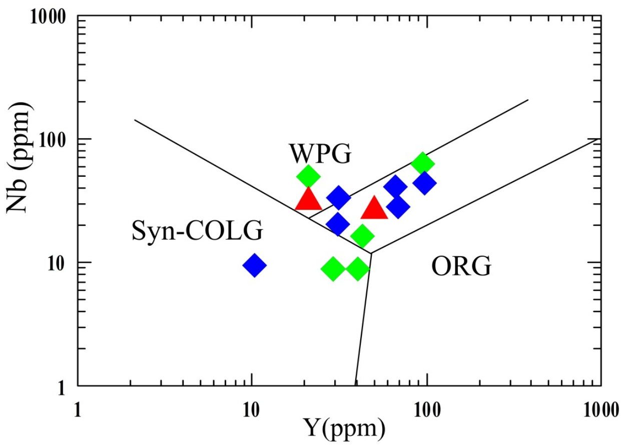

Figure 19. Tectonic discrimination diagram (Nb versus Y) based on [100] for the intrusive rocks. Syn-COLG = syn-collision granite, WPG = within-plate granite, ORG = ocean-ridge granite.

5. Conclusions

The goal of the present investigation was to utilize multiple types of satellite imagery to obtain the most accurate images of the rocks in the area, verifying this separation using petrographical and geochemical studies. According to the remote sensing and laboratory studies, the main types of Precambrian rock units in the region were classified, namely, volcanic-sedimentary sequences, diorite, gabbro, granite, and albitite. To compare the geological map of the study district with the previously published map, several approaches—including fieldwork, petrography, geochemistry, principal component analysis, band ratio, FCC, and MNF images from Landsat-8 photos—were used. The updated map is more precise and effectively distinguishes between the various rock units in the research district. Geological mapping of the Wadi Kid district was established successfully by using different remote sensing techniques—i.e., false color composite (FCC), principal component analysis (PCA), band ratio (BR), and minimum noise fraction (MNF)—on Landsat-8 images. The field study revealed that the main rock units observed in the study district were metasediments, gabbros, diorites, granites, and albitites. The low-grade metamorphosed metasediments were recorded in the central and southeastern parts of the Wadi Kid district, encountered in the Wadi Samra, Wadi Khashm El-Fakh, Wadi Khashm El-Biya, and Wadi Ghorabi El-Hatimyia areas as the Heib and Tarr formations. In the Heib formation, the metasediment succession includes turbiditic slate and graywacke, as well as cobble and boulder conglomerate beds and lenses with clasts, whereas the Tarr formation includes dacite–andesite lavas, ignimbrites, volcanic breccias and tuffs, pebbly mudstones, and impure carbonate minerals. Petrographically, the metasediments are discriminated into tremolite–actinolite schists. Shahira gabbros were recorded in the northeastern part of the study district as medium–coarse-grained, ranging in color from dark to light greenish-gray, and characterized by hydrothermal alterations next to granite intrusions. Meanwhile, the dioritic rocks are characterized as well exposed in Wadi Kid and the east Qabila district, and close to the contact with the granites they are represented by syenogranites exposed in the Wadi Qabila east and Kid districts that are stained red and in sharp contact with diorites and Dokhan volcanics. The main body of albitites ($\approx$1.2 km^2) occurs as small and brecciated irregular intrusions encountered upstream of Wadi Tarr, as well as at Wadi Samra, Wadi Khashm El-Fakh, and Wadi Ghorabi El-Hatimyia. The common hydrothermal alterations include petrographic carbonatization, silicification, sericitization, kaolinitization, and chloritization. Geochemically, the studied rocks are classified into metasedimentary rocks and intrusive rocks (e.g., diorites, granites, and albitites). The metasediments belong to pelitic graywackes originally from shales and characterized by high MgO contents and low SiO_2, Fe_2O_3, and CaO contents. All of the metasediments show a peraluminous character with an $Al_2O_3/(CaO+Na_2O+K_2O)$ ratio higher than 1 (1.30–2.02). Granitic rocks are classified as having alkaline and subalkaline (high-K calc-alkaline–shoshonite series) affinity. Alkaline rocks are classified as albitite, while the calc-alkaline series samples vary from monzodiorites to granites in composition. The results of this investigation can be used for future metallic and industrial mineral exploration in the Wadi Kid district. According to geochemical analyses, the syenites, monzodiorites, and granites in the Kid region vary from metaluminous to peraluminous rock series, and they formed during syn-collision and within a plate environment.

Author Contributions: Conceptualization, W.F., H.M.E.-D., M.H.E. and A.S. (Aref Shirazi); methodology, P.A.K., H.E.-A., A.M.A.-R., A.E.K., A.S. (Adel Shirazy) and A.H.; supervision, A.E., A.B.P., A.S. (Adel Shirazy), A.S. (Aref Shirazi) and W.F. All authors have read and agreed to the published version of the manuscript.

Funding: This research received no external funding.

Conflicts of Interest: The authors declare no conflict of interest.

References

1. Ninomiya, Y.; Fu, B.; Cudahy, T.J. Detecting lithology with Advanced Spaceborne Thermal Emission and Reflection Radiometer (ASTER) multispectral thermal infrared "radiance-at-sensor" data. *Remote Sens. Environ.* **2005**, *99*, 127–139. [CrossRef]
2. Safari, M.; Maghsoudi, A.; Pour, A.B. Application of Landsat-8 and ASTER satellite remote sensing data for porphyry copper exploration: A case study from Shahr-e-Babak, Kerman, south of Iran. *Geocarto Int.* **2018**, *33*, 1186–1201. [CrossRef]
3. Bachri, I.; Hakdaoui, M.; Raji, M.; Teodoro, A.C.; Benbouziane, A. Machine learning algorithms for automatic lithological mapping using remote sensing data: A case study from Souk Arbaa Sahel, Sidi Ifni Inlier, western anti-Atlas. *Moroc. Int. J. Geoinf.* **2019**, *8*, 248. [CrossRef]

4. Beiranvand Pour, A.; Park, Y.; Crispini, L.; Läufer, A.; Kuk Hong, J.; Park, T.Y.; Zoheir, B.; Pradhan, B.; Muslim, A.M.; Hossain, M.S.; et al. Mapping listvenite occurrences in the damage zones of Northern Victoria Land, Antarctica using ASTER satellite remote sensing data. *Remote Sens.* **2019**, *11*, 1408. [CrossRef]
5. Mushore, T.D.; Odindi, J.; Dube, T.; Matongera, T.N.; Mutanga, O. Remote sensing applications in monitoring urban growth impacts on in-and-out door thermal conditions: A review. *Remote Sens. Appl. Soc. Environ.* **2017**, *8*, 83–93. [CrossRef]
6. Zhang, X.; Li, P. Lithological mapping from hyperspectral data by improved use of spectral angle mapper. *Int. J. Appl. Earth Obs. Geoinf.* **2014**, *31*, 95–109. [CrossRef]
7. Masoumi, F.; Eslamkish, T.; Abkar, A.A.; Honarmand, M.; Harris, J.R. Integration of spectral, thermal, and textural features of ASTER data using Random Forests classification for lithological mapping. *J. Afr. Earth Sci.* **2017**, *129*, 445–457. [CrossRef]
8. Pour, A.B.; Hashim, M.; Park, Y.; Hong, J.K. Mapping alteration mineral zones and lithological units in Antarctic regions using spectral bands of ASTER remote sensing data. *Geocarto Int.* **2018**, *33*, 1281–1306. [CrossRef]
9. Zoheir, B.; El-Wahed, M.A.; Pour, A.B.; Abdelnasser, A. Orogenic gold in transpression and transtension zones: Field and remote sensing studies of the barramiya–mueilha sector, Egypt. *Remote Sens.* **2019**, *11*, 2122. [CrossRef]
10. Zamyad, M.; Afzal, P.; Pourkermani, M.; Nouri, R.; Jafari, M.R. Determination of hydrothermal alteration zones using remote sensing methods in Tirka Area, Toroud, NE Iran. *J. Indian Soc. Remote Sens.* **2019**, *47*, 1817–1830. [CrossRef]
11. Zoheir, B.; Emam, A. Field and ASTER imagery data for the setting of gold mineralization in Western Allaqi–Heiani belt, Egypt: A case study from the Haimur deposit. *J. Afr. Earth Sci.* **2014**, *99*, 150–164. [CrossRef]
12. Sadek, M.F.; Ali-Bik, M.W.; Hassan, S.M. Late Neoproterozoic basement rocks of Kadabora-Suwayqat area, Central Eastern Desert, Egypt: Geochemical and remote sensing characterization. *Arab. J. Geosci.* **2015**, *8*, 10459–10479. [CrossRef]
13. Kamel, M.; Abu El Ella, E.S.M. Integration of Remote Sensing & GIS to Manage the Sustainable Development in the Nile Valley desert fringes of assiut-sohag governorates, upper Egypt. *J. Indian Soc. Remote Sens.* **2016**, *44*, 759–774.
14. Aboelkhair, H.; Abdelhalim, A.; Hamimi, Z.; Al-Gabali, M. Reliability of using ASTER data in lithologic mapping and alteration mineral detection of the basement complex of West Berenice, Southeastern Desert. *Egypt. Arab. J. Geosci.* **2020**, *13*, 287. [CrossRef]
15. Hamimi, Z.; Hagag, W.; Kamh, S.; El-Araby, A. Application of remote-sensing techniques in geological and structural mapping of Atalla Shear zone and environs, central Eastern Desert. *Egypt. Arab. J. Geosci.* **2020**, *13*, 414. [CrossRef]
16. Ali-Bik, M.W.; Hassan, S.M.; Sadek, M.F. Volcanogenic talc-copper deposits of Darhib-Abu Jurdi area, Egypt: Petrogenesis and remote sensing characterization. *Geol. J.* **2020**, *55*, 5330–5354. [CrossRef]
17. Asran, A.M.; Hassan, S.M. Remote sensing-based geological mapping and petrogenesis of Wadi Khuda Precambrian rocks, South Eastern Desert of Egypt with emphasis on leucogranite. *Egypt. J. Remote Sens. Space Sci.* **2021**, *24*, 15–27. [CrossRef]
18. Shokry, M.M.; Sadek, M.F.; Osman, A.F.; El Kalioubi, B.A. Precambrian basement rocks of Wadi-Khuda-Shut area, South Eastern Desert of Egypt: Geology and remote sensing analysis. *Egypt. J. Remote Sens. Space Sci.* **2021**, *24*, 59–75. [CrossRef]
19. Shebl, A.; Abdellatif, M.; Hissen, M.; Abdelaziz, M.I.; Csamer, A. Lithological mapping enhancement by integrating Sentinel 2 and gamma-ray data utilizing support vector machine: A case study from Egypt. *Int. J. Appl. Earth Obs. Geoinf.* **2021**, *105*, 102619. [CrossRef]
20. Soliman, N.M.; El-Desoky, H.M.; Heikal, M.A.; Abdel-Rahman, A.M. Using ASTER images and field work data for geological mapping around Wadi Umm Ashira and Wadi Tilal Al-Qulieb, Northwestern part of Wadi Allaqi, South Eastern Desert, Egypt. *Arab. J. Geosci.* **2021**, *14*, 1826. [CrossRef]
21. EEl-Desoky, H.M.; Tende, A.W.; Abdel-Rahman, A.M.; Ene, A.; Awad, H.A.; Fahmy, W.; El-Awny, H.; Zakaly, H.M. Hydrothermal alteration mapping using landsat 8 and ASTER data and geochemical characteristics of Precambrian rocks in the Egyptian shield: A Case Study from Abu Ghalaga, Southeastern Desert, Egypt. *Remote Sens.* **2022**, *14*, 3456. [CrossRef]
22. Khedr, M.Z.; Abo Khashaba, S.M.; El-Shibiny, N.H.; El-Arafy, R.A.; Takazawa, E.; Azer, M.K.; Pallin, M. Remote sensing techniques and geochemical constraints on the formation of the Wadi El-Hima mineralized granites, Egypt: New insights into the genesis and accumulation of garnets. *Int. J. Earth Sci.* **2022**, *111*, 2409–2443. [CrossRef]
23. Khashaba, S.M.A.; El-Shibiny, N.H.; Hassan, S.M.; Takazawa, E.; Khedr, M.Z. Application of remote sensing data integration in detecting mineralized granitic zones: A case study of the Gabal Al-Ijlah Al-Hamra, Central Eastern Desert, Egypt. *J. Afr. Earth Sci.* **2023**, *200*, 104855. [CrossRef]
24. Zhang, T.; Yi, G.; Li, H.; Wang, Z.; Tang, J.; Zhong, K.; Li, Y.; Wang, Q.; Bie, X. Integrating Data of ASTER and Landsat-8 OLI (AO) for Hydrothermal Alteration Mineral Mapping in Duolong Porphyry Cu-Au Deposit, Tibetan Plateau, China. *Remote Sens.* **2016**, *8*, 890. [CrossRef]
25. Bouwafoud, A.; Mouflih, M.; Benbouziane, A. Lithological Mapping Using Landsat 8 OLI in the Meso-Cenozoic Tarfaya Laayoune Basin (South of Morocco): Comparison between ANN and SID Classification. *Open J. Geol.* **2021**, *11*, 658–681. [CrossRef]
26. Patchett, P.J.; Chase, C.G. Role of transform continental margins in major crustal growth episodes. *Geology* **2002**, *30*, 39–42. [CrossRef]
27. Stern, R.J. Arc assembly and continental collision in the Neoproterozoic East African Orogen: Implications for the consolidation of Gondwanaland. *Annu. Rev. Earth Planet Sci.* **1994**, *22*, 319–351. [CrossRef]
28. Stern, R.J. Crustal evolution in the East African Orogen: A neodymium isotopic perspective. *J. Afr. Earth Sci.* **2002**, *34*, 109–117. [CrossRef]
29. Stern, R.J. Subduction zones. *Rev. Geophys.* **2002**, *40*, 3–38. [CrossRef]

30. Stern, R.J. Neoproterozoic crustal growth: The solid earth system during a critical episode of Earth history. *Gondwana Res.* **2008**, *14*, 33–50. [CrossRef]
31. Hargrove, U.S.; Stern, R.J.; Kimura, J.I.; Manton, W.I.; Johnson, P.R. How juvenile is the Arabian-Nubian Shield? Evidence from Nd isotopes and pre-Neoproterozoic inherited zircon in the Bi'r Umq suture zone, Saudi Arabia. *Earth Planet Sci. Lett.* **2006**, *252*, 308–326. [CrossRef]
32. Vaughan, A.P.M.; Pankhurst, R.J. Tectonic overview of the West Gondwana margin. *Gondwana Res.* **2008**, *13*, 150–162. [CrossRef]
33. Avigad, D.; Gvirtzman, Z. Late Neoproterozoic Arabian—Rise and fall of the northern Nubian Shield: The role of lithospheric mantle delamination and subsequent thermal subsidence. *Tectonophysics* **2009**, *477*, 217–228. [CrossRef]
34. Johnson, P.R.; Andresen, A.; Collins, A.S.; Fowler, A.R.; Fritz, H.; Ghebreab, W.; Kusky, T.; Stern, R.J. Late Cryogenian-Ediacaran history of the Arabian-Nubian Shield: A review of depositional, plutonic, structural, and tectonic events in the closing stages of the northern East African Orogen. *J. Afr. Earth Sci.* **2011**, *61*, 167–232. [CrossRef]
35. Be'eri-Shlevin, Y.; Eyal, M.M.; Eyal, Y.; Whitehouse, M.J.; Litvinovsky, B. The Sa'al volcano-sedimentary complex (Sinai, Egypt), a latest Mesoproterozoic volcanic arc in the northern Arabian-Nubian Shield. *Geology* **2012**, *40*, 403–406. [CrossRef]
36. Fritz, H.; Abdelsalam, M.; Ali, K.A.; Bingen, B.; Collins, A.S.; Fowler, A.R.; Ghebreab, W.; Hauzenberger, C.A.; Johnson, P.R.; Kusky, T.M.; et al. Orogen styles in the East African Orogen: A review of the Neoproterozoic to Cambrian tectonic evolution. *J. Afr. Earth Sci.* **2013**, *86*, 65–106. [CrossRef] [PubMed]
37. El-Bialy, M.Z.; Hassen, I.S. The late Ediacaran (580–590 Ma) onset of anorogenic alkaline magmatism in the Arabian-Nubian Shield: Katherina A-type rhyolites of Gabal Ma'ain, Sinai, Egypt. *Precambrian Res.* **2012**, *216*, 1–22. [CrossRef]
38. Azer, M.K.; Obeid, M.A.; Gahlan, H.A. Late Neoproterozoic layered mafic intrusion of arc-affinity in the Arabian-Nubian Shield: A case study from the Shahira layered mafic intrusion, southern Sinai, Egypt. *Geol. Acta Int. Earth Sci. J.* **2016**, *14*, 237–259.
39. El-Bialy, M.Z.; Shata, A.E. Geochemistry, petrogenesis and radioactive mineralization of two coeval Neoproterozoic post-collisional calc-alkaline and alkaline granitoid suites from Sinai, Arabian Nubian Shield. *Chem. Erde* **2018**, *78*, 15–39. [CrossRef]
40. Fowler, A.; Hassen, I.S.; Hassan, M. The Feiran-Solaf metamorphic complex, Sinai, Egypt: Evidence for orthogonal or oblique tectonic convergence? *J. Afr. Earth Sci.* **2017**, *146*, 48–65. [CrossRef]
41. Azer, M.K.; Gahlan, H.A.; Asimow, P.D.; Al-Kahtany, K.M. The common origin and alteration history of the hypabyssal and volcanic phases of the Wadi Tarr Albitite Complex, southern Sinai, Egypt. *Lithos* **2019**, *324*, 821–841. [CrossRef]
42. Morad, A.E.; Abdelrahman, H.B.; Ali, M.S.; Ali, S. Metamorphic conditions and igneous activity in the Um Zariq area, East Sinai, Egypt: Mineralogical and petrological evidences for the transformation from collisional to an extensional regime in the Arabian-Nubian shield. *J. Afr. Earth Sci.* **2021**, *182*, 104302. [CrossRef]
43. Helmy, M.H.; Morad, E.A.; Abdel Rahman, B.H. Um Zariq formation, southeast sinai, Egypt: A new record of the Sturtian Snowball Earth event in the Arabian Nubian Shield. *J. Afr. Earth Sci.* **2021**, *173*, 104048. [CrossRef]
44. El-Desoky, H.M.; Abdel-Rahman, A.M.; Fahmy, W.; Khalifa, I.; Mohamed, S.A.; Shirazi, A.; Hezarkhani, A.; Shirazy, A.; Pour, A.B. Ore Genesis of the Abu Ghalaga Ferro-Ilmenite Ore Associated with Neoproterozoic Massive-Type Gabbros, South-Eastern Desert of Egypt: Evidence from Texture and Mineral Chemistry. *Minerals* **2023**, *13*, 307. [CrossRef]
45. Moussa, E.M.; Stern, R.J.; Manton, W.I.; Ali, K.A. SHRIMP zircon dating and Sm/Nd isotopic investigations of Neoproterozoic granitoids, Eastern Desert, Egypt. *Precambrian Res.* **2008**, *160*, 341–356. [CrossRef]
46. El-Sayed, M.M.; Mohamed, F.H.; Furnes, H.; Kanisawa, S. Geochemistry and petrogenesis of the Neoproterozoic granitoids in the Central Eastern Desert, Egypt. *Chem. Erde* **2002**, *62*, 317–346. [CrossRef]
47. Farahat, E.S.; Mohamed, H.A.; Ahmed, A.F.; El Mahallawi, M.M. Origin of I-and A-type granitoids from the Eastern Desert of Egypt: Implications for crustal growth in the northern Arabian–Nubian Shield. *J. Afr. Earth Sci.* **2007**, *49*, 43–58. [CrossRef]
48. Abdel-Rahman AF, M.; Martin, R.F. The Mount Gharib A-type granite, Nubian Shield: Petrogenesis and role of metasomatism at the source. *Contrib. Mineral. Petrol.* **1990**, *104*, 173–183. [CrossRef]
49. Abdel-Rahman, A.M.; El-Kibbi, M.M. Anorogenic magmatism: Chemical evolution of the Mount El-Sibai A-type complex (Egypt), and implications for the origin of within-plate felsic magmas. *Geol. Mag.* **2001**, *138*, 67–85. [CrossRef]
50. Mohamed, F.H.; El-Sayed, M.M. Post-orogenic and anorogenic A-type fluorite-bearing granitoids, Eastern Desert, Egypt: Petrogenetic and geotectonic implications. *Chem. Erde* **2008**, *68*, 431–450. [CrossRef]
51. Be'eri-Shlevin, Y.; Katzir, Y.; Valley, J.W. Crustal evolution and recycling in a juvenile continent: Oxygen isotope ratio of zircon in the northern Arabian Nubian Shield. *Lithos* **2009**, *107*, 169–184. [CrossRef]
52. Eyal, M.; Litvinovsky, B.; Jahn, B.M.; Zanvilevich, A.; Katzir, Y. Origin and evolution of post-collisional magmatism: Coeval Neoproterozoic calc-alkaline and alkaline suites of the Sinai Peninsula. *Chem. Geol.* **2010**, *269*, 153–179. [CrossRef]
53. El-Bialy, M.Z.; Omar, M.M. Spatial association of Neoproterozoic continental arc I-type and post-collision A-type granitoids in the Arabian-Nubian Shield: The Wadi Al-Baroud Older and younger granites, North Eastern Desert. *Egypt. J. Afr. Earth Sci.* **2015**, *103*, 1–29. [CrossRef]
54. Shimron, A.E. Late phase deformation and mylonite belts in Sinai: Pan African thrust fault tectonics. *Geol. Surv. Isr.* **1980**, *1*, 75–80.
55. Furnes, H.; Shimron, A.E.; Roberts, D. Geochemistry of Pan-African volcanic arc sequences in southeastern Sinai Peninsula and plate tectonic implications. *Precambrian Res.* **1985**, *29*, 359–382. [CrossRef]
56. Blasband, B.; Brooijmans, P.; Dirks, P.; Visser, W.; White, S. A Pan-African core complex in the Sinai, Egypt. *Geol. Mijnb.* **1997**, *76*, 247–266. [CrossRef]

57. Blasband, B.; White, S.; Brooijmans, P.; De Boorder, H.; Visser, W. Late Proterozoic extensional collapse in the Arabian-Nubian shield. *J. Geol. Soc.* **2000**, *157*, 615–628. [CrossRef]
58. Brooijmans, P.; Blasband, B.; White, S.H.; Visser, W.J.; Dirks, P. Geothermobarometric evidence for a metamorphic core complex in Sinai, Egypt. *Precambrian Res.* **2003**, *123*, 249–268. [CrossRef]
59. Bentor, Y.K.; Bogosh, R.; Eyal, M.; Garfunkel, Z.; Shimron, A. *Geological Map of Sinai, Jebel Sabbagh Sheet, 1:100,000 Scale*; Academy of Science and Humanities: Jerusalem, Israel, 1974.
60. Shimron, A.E.; Arkin, Y. *Precambrian Geology of Wadi Kid-Wadi Umm Adawi Area, Eastern Sinai. Reconnaissance Map 1:25,000 and Explanatory Notes*; Rep. No. MM/1/78; Geological survey of Israel: Jerusalem, Israel, 1978.
61. El-Shafei, M.K.; Kusky, T. Structural and tectonic evolution of the Neoproterozoic Feiran–Solaf metamorphic belt Sinai Peninsula: Implications for the closure of the Mozambique Ocean. *Precambrian Res.* **2003**, *123*, 269–293. [CrossRef]
62. Blasy, M.; El-Baroudy, A.F.; Kharbish, S.M. Geochemical characteristics of Wadi Tarr albitite, southeastern Sinai, Egypt. *Egypt. J. Geol.* **2001**, *45*, 767–780.
63. Fowler, A.; Hassen, I.S.; Osman, A.F. Neoproterozoic structural evolution of SE Sinai, Egypt: II. Convergent tectonic history of the continental arc Kid Group. *J. Afr. Earth Sci.* **2010**, *58*, 526–546. [CrossRef]
64. Abu El-Enen, M.M.; Makroum, F.M. Tectonometamorphic evolution of the northeastern Kid Belt, Southeast Sinai, Egypt. *Ann. Geol. Surv. Egypt* **2003**, *VXXVI*, 19–37.
65. Shimron, A. The Dahab mafic–ultramafic complex, southern Sinai Peninsula: A probable ophiolite of Late Proterozoic (Pan-African) age. *Ofioliti* **1981**, *6*, 161–164.
66. Shimron, A.E. The Tarr Complex revisited folding, thrusts and mélanges in the southern Wadi Kid region, Sinai Peninsula. *Isr. J. Earth Sci.* **1983**, *32*, 123–148.
67. Halpern, M.; Tristan, N. Geochronology of the Arabian-Nubian Shield in southern Israel and eastern Sinai. *J. Geology.* **1981**, *89*, 639–648. [CrossRef]
68. Bielski, M. Stages in the Arabian–Nubian Massif in Sinai. Ph.D. Thesis, Hebrew University, Jerusalem, Israel, 1982; p. 155.
69. Moghazi, A.-K.M.; Ali, K.A.; Wilde, S.A.; Zhou, Q.; Andersen, T.; Andresen, A.; Abu El-Enen, M.M.; Stern, R.J. Geochemistry, geochronology, and Sr–Nd isotopes of the late Neoproterozoic Wadi Kid volcano-sedimentary rocks, Southern Sinai, Egypt: Implications for tectonic setting and crustal evolution. *Lithos* **2012**, *154*, 147–165. [CrossRef]
70. Green, A.A.; Berman, M.; Switzer, P.; Craig, M.D. A transformation for ordering multispectral data in terms of image quality with implications for noise removal. *IEEE Trans. Geosci. Remote Sens.* **1988**, *26*, 65–74. [CrossRef]
71. Roy, D.P.; Wulder, M.A.; Loveland, T.R.; Woodcock, C.E.; Allen, R.G.; Anderson, M.C.; Helder, D.; Irons, J.R.; Johnson, D.M.; Kennedy, R.; et al. Landsat-8: Science and product vision for terrestrial global change research. *Remote Sens. Environ.* **2014**, *145*, 154–172. [CrossRef]
72. Shebl, A.; Csamer, A. Reappraisal of DEMs, radar and optical datasets in lineaments extraction with emphasis on the spatial context. *Remote Sens. Appl. Soc. Environ.* **2021**, *24*, 100617. [CrossRef]
73. Chavez, P.S., Jr.; Berlin, G.L.; Sowers, L.B. Statistical method for selecting Landsat MSS ratios. *J. Appl. Photogr. Eng.* **1982**, *8*, 23–30.
74. Richards, J.A. *Remote Sensing Digital Image Analysis*; Springer: Berlin/Heidelberg, Germany, 1999; p. 3.
75. Boardman, J.W.; Kruse, F.A. Automatic spectral analysis: A geological example using AVIRIS data, North Grapevine mountain, Nevada. In Proceedings of the 10th Thematic Conference on Geologic Remote Sensing, San Antonio, TX, USA, 9–12 May 1994; pp. 407–418.
76. Gupta, R.P. *Remote Sensing Geology*, 2nd ed.; Springer: Berlin/Heidelberg, Germany, 2003; p. 655.
77. Drury, S.A. *Image Interpretation in Geology*, 1st ed.; Allen&Unwin: London, UK, 1987; p. 243.
78. Crane, R.B. Processing techniques to reduce atmospheric and sensorvariability in multispectral scanner data. In Proceedings of the 7th International Symposium on Remote Sensing of Environment. *Ann. Arbor.* **1971**, *2*, 1345–1355.
79. Vincent, R.K. *Fundamentals of Geological and Environmental Remote Sensing*; Prentice-Hall, Inc.: Upper Saddle River, NJ, USA, 1997.
80. Shabani, A.; Ziaii, M.; Monfared, M.S.; Shirazy, A.; Shirazi, A. Multi-Dimensional Data Fusion for Mineral Prospectivity Mapping (MPM) Using Fuzzy-AHP Decision-Making Method, Kodegan-Basiran Region, East Iran. *Minerals* **2022**, *12*, 1629. [CrossRef]
81. Aali, A.A.; Shirazy, A.; Shirazi, A.; Pour, A.B.; Hezarkhani, A.; Maghsoudi, A.; Hashim, M.; Khakmardan, S. Fusion of Remote Sensing, Magnetometric, and Geological Data to Identify Polymetallic Mineral Potential Zones in Chakchak Region, Yazd, Iran. *Remote Sens.* **2022**, *14*, 6018. [CrossRef]
82. Dohuee, M.; Khosravi, V.; Shirazi, A.; Shirazy, A.; Nazerian, H.; Pour, A.B.; Hezarkhani, A.; Pradhan, B. Alteration Detections Using ASTER Remote Sensing data and Fractal Geometry for Mineral prospecting in Hemich Area, NE Iran. In Proceedings of the IGARSS 2022–2022 IEEE International Geoscience and Remote Sensing Symposium, Kuala Lumpur, Malaysia, 17–22 July 2022; pp. 5520–5523.
83. Sabins, F.F. Remote Sensing for mineral exploration. *Ore Geol. Rev.* **1999**, *14*, 157–183. [CrossRef]
84. Lillesand, T.M.; Kiefer, R.W. *Remote Sensing and Image Interpretation*, 3rd ed.; Wiley: New York, NY, USA, 1994; p. 750. [CrossRef]
85. Shirazi, A.; Hezarkhani, A.; Beiranvand Pour, A.; Shirazy, A.; Hashim, M. Neuro-Fuzzy-AHP (NFAHP) Technique for Copper Exploration Using Advanced Spaceborne Thermal Emission and Reflection Radiometer (ASTER) and Geological Datasets in the Sahlabad Mining Area, East Iran. *Remote Sens.* **2022**, *14*, 5562. [CrossRef]
86. Azer, M.K.; Stern, R.J.; Kimura, J.I. Origin of a late Neoproterozoic (605_13 Ma) intrusive carbonate albitite complex in southern Sinai, Egypt. *Int. J. Earth Sci.* **2010**, *99*, 245–267. [CrossRef]

87. El-Nisr, S.A.; Surour, A.A.; Moufti, A.M.B. Geochemistry and petrogenesis of dyke swarms in NWSinai, Egypt: A case of transition fromcompressional to extensional regimes during the late Neoproterozoic. *J. Tethys* **2014**, *2*, 160–177.
88. Streckeisen, A. Plutonic rocks: Classification and nomenclature recommended by the IVGS sub-commission on the systematic of igneous rocks. *Geotimes* **1976**, *18*, 26–30.
89. Pettijohn, F.J.; Potter, P.E.; Siever, R. *Sands and Sandstones*; Springer: New York, NY, USA, 1972; p. 618.
90. Wimmenauer, W. Das prävaristische Kristallin im Schwarzwald. *Fortschr. Miner. Beih.* **1984**, *62*, 69–186.
91. Nockolds, S.R. The relation between chemical composition and paragenesis in the biotites of micas of igneous rocks. *Am. J. Sci* **1947**, *245*, 401–420. [CrossRef]
92. Herron, M.M. Geochemical classification of terrigenous sands and shales from core or log data. *J. Sediment. Res.* **1988**, *58*, 820–829.
93. Peccerillo, A.; Taylor, S.R. Geochemistry of Eocene calc-alkaline volkanic rocks from Kastamonu area, Northern Turkey. *Contrib. Mineral. Petrol.* **1976**, *58*, 63–81. [CrossRef]
94. Abd El Ghaffar, N.I.; El-Bagoury, H.; Ghabrial, D.S.; Abdelwahab, W.; Ismail, A.I. Discrimination of Neoproterozoic granitic-phases in Southern-Sinai, Egypt. Remote sensing, petrography, and geochemistry. *Egypt. J. Remote Sens. Space Sci.* **2021**, *24*, 231–246. [CrossRef]
95. Nedelec, A.; Grujic, D. Un nouvel exemple de magmatisme potassique à ultrapotassique: Les syénites de l'Andringitra (Madagascar). *Earth Planet. Sci.* **2001**, *332*, 739–745.
96. De La Roche, H.; Leterrier, J.; Grondclaude, P.; Marchal, M. A classification of volcanic and plutonic rock using R1-R2 diagrams and major element analyses; Its relationships and current nomenclature. *Chem. Geol.* **1980**, *29*, 183–210. [CrossRef]
97. Frost, B.R.; Barnes, C.G.; Collins, W.J.; Arculus, R.J.; Ellis, D.J.; Frost, C.D. A geochemical classification for granitic rocks. *J. Petrol.* **2001**, *42*, 2033–2048. [CrossRef]
98. Maniar, P.A.; Piccoli, P.M. Tectonic discrimination of granitoids. *Ball. Geol. Soc. Am.* **1989**, *101*, 635–643. [CrossRef]
99. Pearce, J.A.; Harris, N.B.W.; Tindle, A.G. Trace element discrimination diagrams for the tectonic interpretation of granitic rocks. *J. Petrol.* **1984**, *25*, 956–983. [CrossRef]
100. Eby, G.N. The A-type granitoids: A review of their occurrence and chemical characteristics and speculations on their petrogenesis. *Lithos* **1990**, *26*, 115–134. [CrossRef]
101. Eby, N. Chemical subdivision of the A-type granitoids: Petrogenetic and tectonic implications. *Geology* **1992**, *20*, 641–644. [CrossRef]